Control of electrically and optically active structural disorder in 2D transition metal dichalcogenides

Citation for the original published paper (version of record):
Zeng, L., Olsson, E. (2026). Control of electrically and optically active structural disorder in 2D transition metal
dichalcogenides. npj 2D Materials and Applications, 10(1).
http://dx.doi.org/10.1038/s41699-025-00645-2

npj | 2D materials and applications

Review

Published in partnership with FCT NOVA with the support of E-MRS

https://doi.org/10.1038/s41699-025-00645-2

Control of electrically and optically active structural disorder in 2D transition metal dichalcogenides

Lunjie Zeng ✉ & Eva Olsson ✉

Structural disorder affects the electronic structures of 2D TMDs, offering active control of their electrical and optical properties. The control requires knowledge about the correlation between structure and properties, and also techniques for introducing and stabilizing the structural disorder. The recent significant progress shows that the tunability of the structural disorder enables new functionalities of the 2D TMDs. Here we provide an up-to-date review of the current developments.

Initiated by the fabrication and characterization of the electronic properties of graphene[1–3], atomically thin two-dimensional (2D) materials have attracted tremendous research interest over the last two decades, due to a range of fascinating phenomena and outstanding properties discovered in these materials that are not available in their bulk counterparts[1,3–12]. Atomically thin transition metal dichalcogenides (TMDs) are among the most widely studied 2D materials due to their unique physical properties, especially exceptional electrical and optical properties[6,13–20,20,21]. Bulk TMDs, such as MoS_2, $MoSe_2$, WS_2, and WSe_2, are crystals with layered structures in which there is strong in-plane covalent bonding and weak inter-plane van der Waals (vdW) bonding between atomic layers. The weak vdW interlayer coupling allows the separation of individual atomic layers from bulk crystals using mechanical or chemical means[22–24]. Bottom-up growth of atomically thin TMDs crystals by thin film growth techniques has also been extensively explored[25,26].

Quantum confinement plays an important role in the electronic structure and properties of 2D TMDs[6,27]. Monolayer TMDs, such as MoS_2, $MoSe_2$, WS_2, and WSe_2, are direct gap semiconductors with optical gaps in the visible and near-infrared spectral range[14,18,28]. As the number of atomic layers increases, the bandgap decreases and changes to indirect. TMDs also have fascinating excitonic properties, as well as spin and valley states in their band structures[12,14,20,29–31]. The unique and tunable band structures and thickness of 2D TMDs provide an intriguing platform for the realization of a range of excellent electrical and optical functionalities for applications in electronics, optics, and optoelectronics[12,14,20,30–34]. Furthermore, the possibility of assembling 2D vdW structures layer by layer enables an exciting tuning parameter for fabricating and engineering materials and devices with unique and exotic performance[35,36].

The high degree of crystallinity of the 2D TMDs is normally the basis for many of their favorable mechanical, electrical, and optical properties. However, structural disorder and defects that disrupt the ordered lattice and bonding are unavoidable in real materials. The electrical and optical properties of 2D TMDs sensitively depend on the form and distribution of various structural imperfections and heterogeneities. Due to their ultimately small thicknesses and quantum confinement effects in thin 2D TMDs, defects play an even larger role in determining their electrical and optical properties[37–41], compared to bulk materials. The study of structural disorder and defects has been an important and ingrained part of the research endeavor on 2D TMDs since their discovery[42–44], with the aim to better understand the effects of structural disorder on the properties of 2D TMDs, as well as to explore new functionalities[40].

In this review, we will provide a comprehensive review of the up-to-date literature concerning the control of structural disorders that are of critical importance for tailoring the electrical and optical properties of 2D TMDs. We first provide a survey of the characteristics of the different types of electrically and optically active defect structures found in 2D TMDs (Fig. 1a–f). The atomic-scale structural characteristics of the structural disorder, as well as the effect of each type of structural disorder on the electronic and optical properties of 2D TMDs, are discussed (Fig. 1g–i). Thereafter follows a description of the state-of-the-art techniques and methods that are used to create and control the structural disorder (Fig. 1j–l). Advances in developing techniques for controlling structural disorder during material fabrication, as well as post-fabrication are discussed. Finally, an outlook for future research is provided.

Characteristics of electrically and optically active structural defects in 2D TMDs

In this section, the structural characteristics of the different types of structural disorder, as well as the effect of each type of structural disorder on the electronic and optical properties of 2D TMDs, are described. We focus on the 2D TMDs that are most intensively studied. They are in the form of MX_2, with M denoting a transition metal from group VI (Mo and W) and X a chalcogen atom (S, Se, or Te). There are different ways in which the perfect crystalline order can be disrupted and reorganized in 2D TMDs. In an analogy to 3D materials, the most common intrinsic structural defects in 2D materials are 0D (point) defects and 1D (line) defects within the 2D atomic lattice (Fig. 1). Moreover, lattice distortion and structural disorder can also

Department of Physics, Chalmers University of Technology, Gothenburg, Sweden. ✉e-mail: lunjie@chalmers.se; eva.olsson@chalmers.se

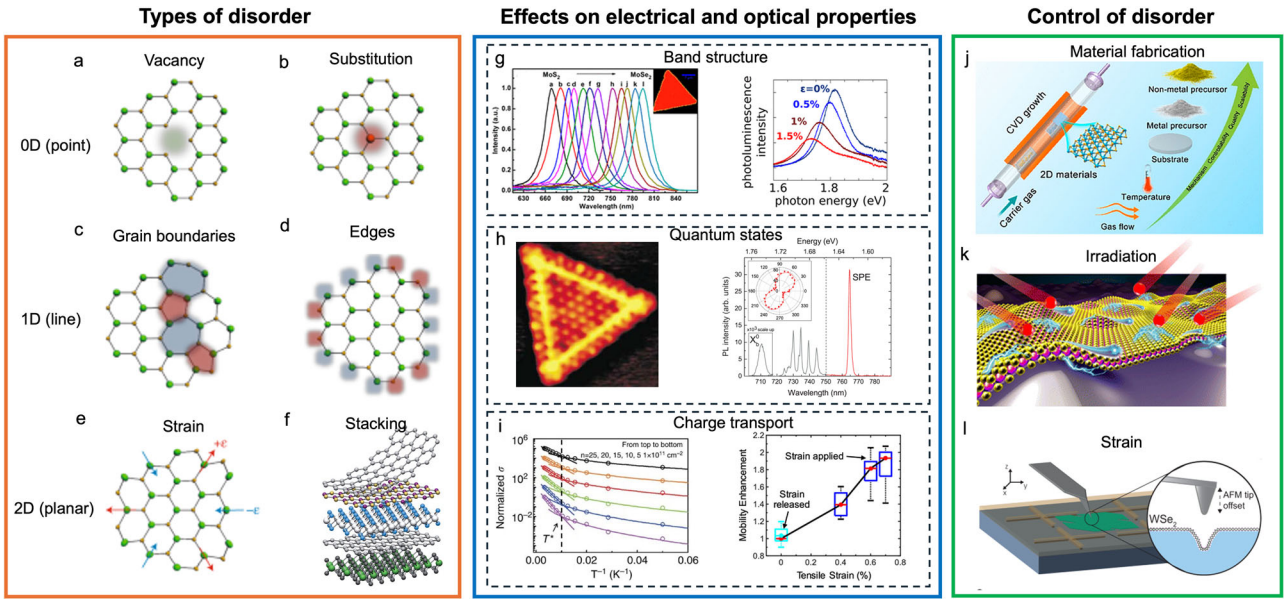

Fig. 1 | Electrically and optically active structural disorder in 2D TMDs. The left panel shows schematics of common electrically and optically active structural disorder and defects in 2D TMDs[35,40]: **a** Vacancy, **b** substitution, **c** grain boundary, **d** edges, **e** strain, **f** stacking disorder. Vacancy and substitution are classified as 0D or point defects. Grain boundary and edge belong to the category of 1D or line defects. 2D or planar disorder includes lattice strain and stacking disorder[35]. The middle panel shows examples of effects of disorder on electrical and optical properties of 2D TMDs: **g** band structure tuning by substitution (left)[86] and lattice strain (right)[188]. **h** Quantum states, including single photo emitters (SPE), created at edges (left)[150] and by atomic scale vacancies and strain (right)[200]. **i** Effects of vacancies (left)[70] and lattice strain (right)[189] on conductivity and charge mobility in 2D TMDs. The structural characteristics of the disorder and their effects on the electrical and optical properties of 2D TMDs are described in the section "Characteristics of electrically and optically active structural defects in 2D TMDs." The panel to the right shows three representative methods to control structural disorder in 2D TMDs: **j** control disorder during the fabrication of 2D TMDs. Chemical vapor deposition (CVD) is a widely used technique to grow 2D TMDs[210]. Growth parameters such as temperature, gas flow, substrate, and precursors can be used to tune the structural disorder. **k** Post-fabrication processing methods, such as irradiation, are often used to generate and manipulate structural disorder in 2D TMDs[264,288,289,290,291]. The irradiation sources can be energetic electrons, ions, plasmas, or photons. **l** Strain engineering, using for example, a scanning probe microscope (SPM), has been utilized to apply and control lattice strain in 2D TMDs[200]. More details of the techniques used for controlling structural disorder are discussed in the section "Control of structural disorder".

involve atoms in one or more atomic layers (Fig. 1). We classify these structural disorders as 2D (planar) defects. One example is lattice strain in 2D TMDs[45]. When the individual atomic layers are stacked together to form 2D vdW structures, structural disorder may emerge due to the variation and inhomogeneity in layer stacking[46–51].

Structure defects and disorder, which often originate from material reorganization and fluctuation at the atomic scale, have been investigated and characterized by a broad range of experimental techniques, including Raman spectroscopy[52,53], X-ray photoelectron spectroscopy (XPS)[54], X-ray diffraction[55], electron microscopy[42], and scanning probe microscopy (SPM)[56]. While methods such as Raman spectroscopy and XPS can be used to study extended and embedded defects, the direct observation and monitoring of defects in 2D materials have been enabled by advanced high-resolution microscopy and spectroscopy techniques, in particular, scanning transmission electron microscopy (STEM) and scanning tunneling microscopy (STM). Modern STEM instrumentation allows direct imaging of atomic structures down to the sub-Å level thanks to the development of spherical and higher-order aberration correctors[57–60]. The unmatched high spatial resolution and versatile functionality for performing atomic resolution imaging, diffraction, and spectroscopy in the same instrument make STEM an indispensable tool for studying defect structures in 2D TMDs. STM is a powerful technique that allows direct atomic resolution imaging as well as electronic structure investigation of the material surface. As a result, STEM and STM have been predominantly used to directly and unambiguously characterize structural disorder down to the atomic scale. In this review, we focus on STEM and STM results when discussing the atomic-scale structure motifs of disorder in 2D TMDs.

Point defects and their effect on electrical and optical properties

Similar as in 3D materials, point defects are probably the most studied structural disorder in 2D TMDS. Point defects may manifest by the missing of individual atoms on certain atomic sites (vacancies), the substitution of atoms by other species (substitutions and dopants), interstitial atoms, as well as adatoms attached to the atomic sites on the 2D lattice. The most profound electrically and optically active point defects in atomically thin TMDs are vacancies and substitutional atoms. In the following, we summarize the advancement in the understanding of the structural characteristics of vacancies and substitution atoms, as well as their effect on the electrical and optical properties of 2D TMDs.

Vacancies and their effect on electrical and optical properties. A vacancy is one of the most prevalent intrinsic defects found in 2D TMDs[38,43,61–66]. Both chalcogen and transition metal atoms can be missing, forming vacancies in 2D TMDs[39,61,64]. Four distinct types of intrinsic vacancies have been identified: mono-chalcogen vacancies (V_X), di-chalcogen vacancies (V_{X2}), vacancy complexes of a transition metal (M) and nearby three chalcogen atoms (V_{MX3}), vacancy complexes with a transition metal and nearby three di-chalcogen pairs (V_{MX6}) (Fig. 2a)[43,61,67]. Antisite defects, where a transition atom occupies a chalcogen site or vice versa, can also be associated with the creation of vacancies. Among these variations, V_X vacancy has the smallest forming energy, making it the most observed point defect in 2D TMDs[38,43,61,63,66]. The methods and techniques used for fabricating 2D TMDs strongly impact the type and density of vacancies[38,39,43,61,63,63–65]. The density of vacancies is normally quite high in the as-prepared 2D crystals, in a range from 10^{12} to above 10^{13} cm^{-2} (Fig. 2b)[61,63,64].

Vacancies significantly affect the electronic properties of 2D TMDs by altering their band structure and introducing localized states (Fig. 2c)[68]. Single vacancies can induce doping in 2D TMDs, increasing charge carrier concentration[69,70]. It is normally believed that chalcogen vacancies in 2D TMDs introduce unpaired electrons into the lattice, n-doping the material, while transition metal vacancies cause p-doping[39,66,70–72]. In the presence of

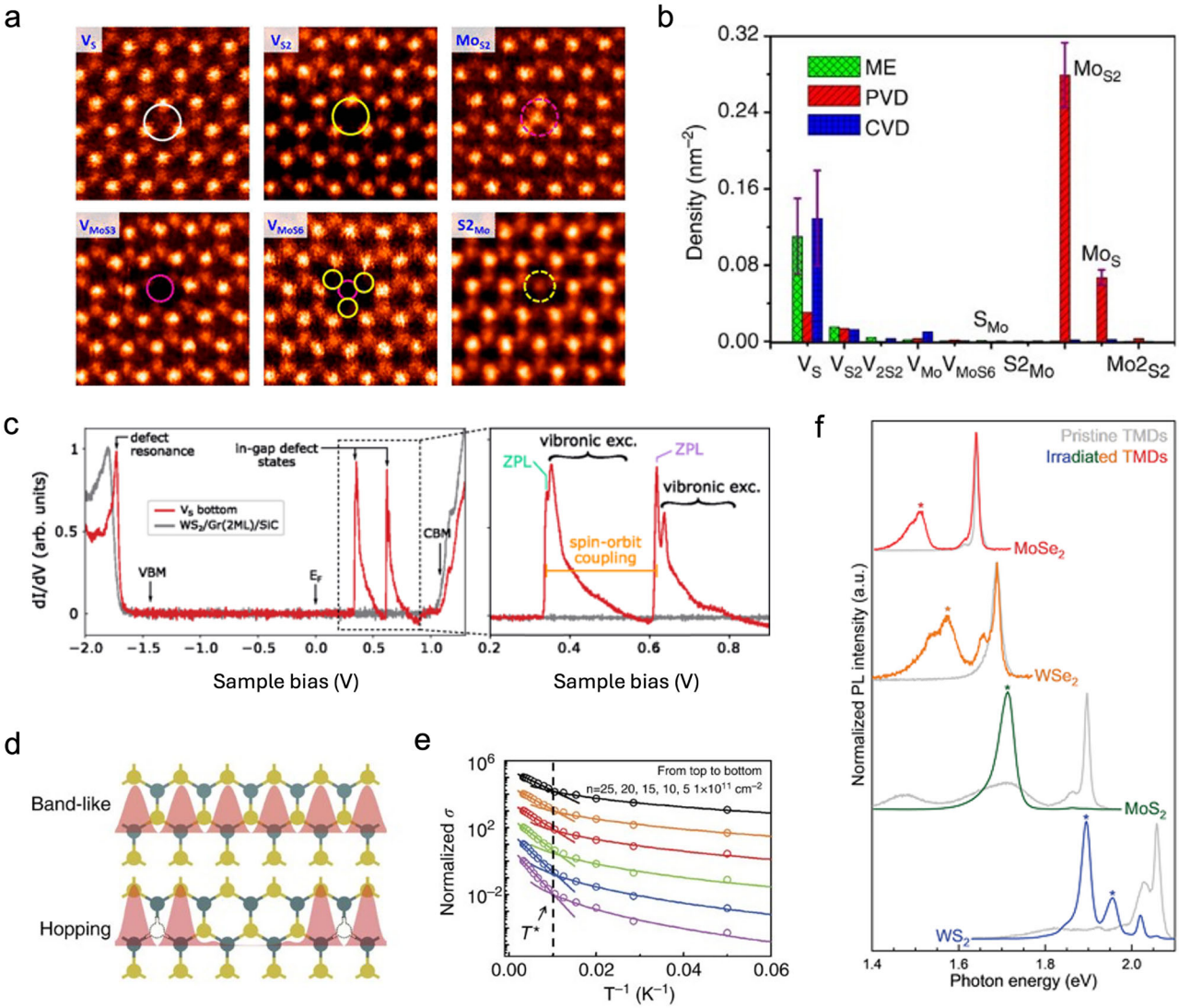

Fig. 2 | Vacancies in 2D TMDs. a Atomic resolution STEM annular dark field (ADF) images of various point defects present in monolayer MoS_2, including monosulphur vacancy (V_S), disulphur vacancy (V_{S2}), vacancy complex of Mo and nearby three sulfur (V_{MoS3}), vacancy complex of Mo nearby three disulphur pairs (V_{MoS6}), and antisite defects where a Mo adatom substituting a S_2 column (Mo_{S2}) or a S_2 column substituting a Mo atom ($S2_{Mo}$)[41]. **b** Statistics of various point defects in physical vapor deposition (PVD), chemical vapor deposition (CVD), and mechanical exfoliation (ME) MoS_2 monolayers. ME data are in green, PVD data in red, and CVD data in blue[61]. **c** Left: scanning tunneling spectroscopy (STS) spectra recorded on a sulfur bottom vacancy and the pristine WS_2 monolayer on bilayer graphene. The valence band maximum (VBM), conduction band minimum (CBM), the Fermi level (EF), the filled-state defect resonance, and the unoccupied in-gap defect states are indicated. Right: Zoom-in view of the STS spectra of the deep unoccupied V_S defect states. The two zero-phonon lines (ZPLs) and the subsequent vibronic satellite peaks are labeled[68]. **d** Schematics of the electron transport mechanism in perfect and defective MoS_2. In perfect MoS_2, transport is band-like. In MoS_2 with vacancies, however, electrons are localized near the defects and transport is through hopping[70]. **e** Arrhenius plot of normalized conductivity (symbols) of monolayer MoS_2 and the fitting results by the hopping model (lines). From top to bottom, carrier density $n = 25, 20, 15, 10, 5, 1 \times 10^{11}$ cm^{-2}, respectively. The two hopping regimes are separated by T* (dashed vertical line)[70]. **f** PL spectra of proton beam irradiated WS_2, MoS_2, WSe_2, and $MoSe_2$ monolayers[73]. Normalized PL spectra of MX_2 monolayers before (gray plots) and after (color plots) irradiation.

single vacancies, charge conduction is believed to be realized by hopping between the localized states introduced by vacancies (Fig. 2d, e)[70,72]. However, when vacancy density is high, vacancy-induced local potential variation and charge states enhance charge scattering, degrading charge transport properties[64].

Chalcogen vacancies are optically active, giving rise to spectrum features at an energy slightly below the natural exciton peak in photoluminescence (PL) of MoS_2, WS_2, $MoSe_2$, and WSe_2 monolayers (Fig. 2f)[73,74]. Defect-bound excitons in monolayer WSe_2 exhibit exceptional optical properties, including a recombination lifetime approaching 200 ns and a valley lifetime longer than 1 μs[75]. Vacancies can also subtly modify the dielectric functions at low dimensionality, causing renormalization of quasiparticle binding energies[76]. Quantum optical phenomena, such as single photon emitters (SPEs), have been widely observed in 2D TMDs[77–80]. Though the precise microscopic structure origin of SPE is still under debate, many studies strongly indicate that chalcogen vacancies are an important source for SPE[81–84].

Atomic substitution and its effect on electrical and optical properties. Atomic substitution is commonly found in 2D TMDs, where both the transition metal and the chalcogen atoms can be replaced by other elements[85]. The most common way of incorporating substitution atoms in 2D TMDs is using the atoms in the same group of the periodic table with similar radius, valence, and coordination (Fig. 3a)[86–97]. The choice of

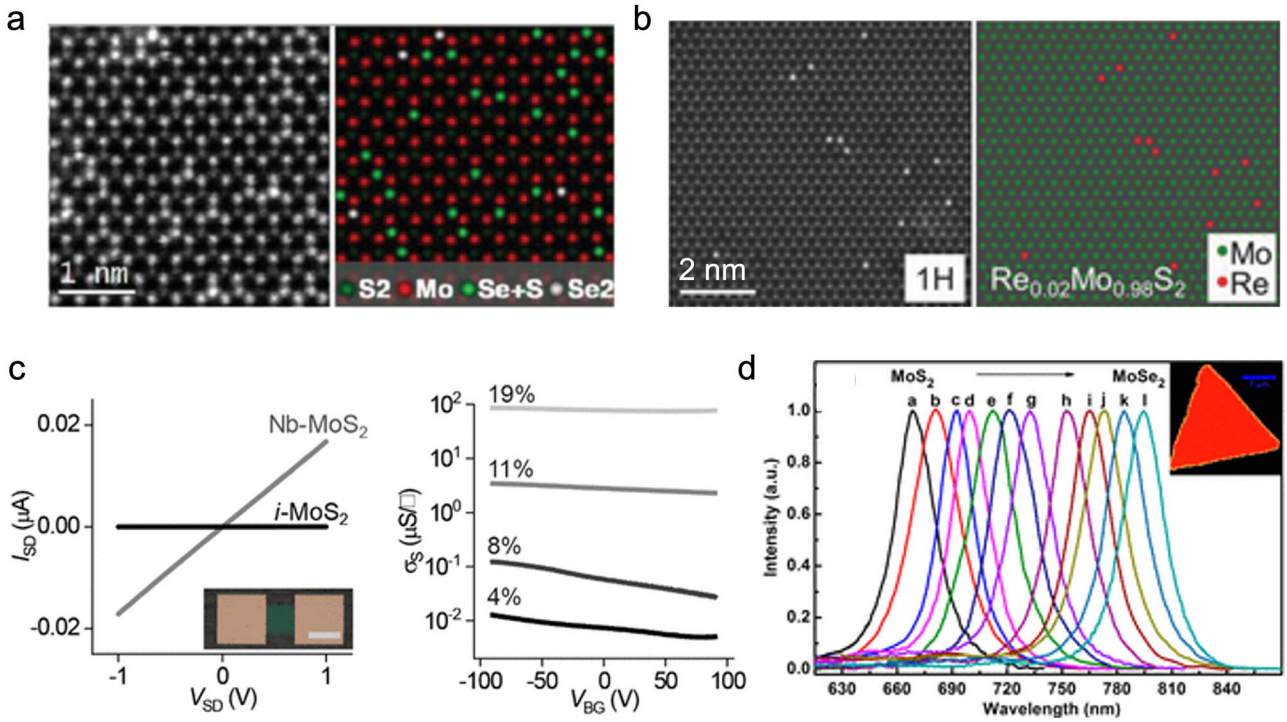

Fig. 3 | Atomic substitution in 2D TMDs. a Atomic resolution STEM ADF image of $MoS_{2x}Se_{2-2x}$ (left) and atom-by-atom structural model (right) obtained from the STEM image[97]. **b** Experimental STEM ADF image (left) of $Re_xMo_{1-x}S_2$ alloy monolayers and the corresponding atom mapping image (right)[98]. **c** Left: *I*–*V* curves of representative undoped-MoS_2 and Nb-MoS_2 (4% Nb). Inset: Optical micrograph of a representative device. Scale bar: 200 μm. The as-fabricated undoped-MoS_2 monolayer devices do not show notable electrical conduction[121]. Right: Transfer curves of Nb-MoS_2 devices at different Nb concentrations. Without doping, the measured sheet conductance, σ_S, is below 10^{-5} μS/□. With Nb doping, the devices exhibit a much higher conductance ($\sigma > 10^{-2}$ μS/□) for a doping concentration of 4%. Doped MoS_2 shows a p-type V_{BG} (back gate voltage) dependence[121]. **d** PL spectra of the complete composition $MoS_{2x}Se_{2(1-x)}$ nanosheets and a typical PL mapping of a single ternary nanosheet (the inset, scale bar, 7 μm), excited with a 488 nm argon ion laser[86].

dopant elements has been extended to transition metal elements in other transition metal groups of the periodic table as well. For example, Mn and Re from group VII have been used to dope MoS_2 (Fig. 3b)[98–100]. Nb and V, from group V of the periodic table, have been added into the WS_2 lattice, replacing W atoms[101–105]. Though less common, other transition metals, such as Cr, Fe, Ni, Mn, and Co, have also been used to substitute W or Mo in 2D TMDs[99,105–107]. Both the transition metal and chalcogen dopants are often randomly dispersed in the 2D lattice[93,94], but clusters have also been observed in some systems, especially at high dopant concentrations[108].

Rare-earth elements have also been used as substitution elements for 2D TMDs, replacing the transition metal atoms. Er- and Yb- substitution has been introduced in MoS_2 and WS_2 nanosheets, as well as monolayers[109–116]. Ce-substitution has been realized in WS_2 monolayers[117]. Er/Yb co-doped WS_2 monolayers have been fabricated[118]. Substitution of 2D TMDs with other lanthanoid atoms, such as La, Pr, Nd, Sm, and Eu, has also been realized[119].

Doping can be introduced by substituting elements in 2D TMDs using elements from different groups than those in the original materials, influencing carrier type and concentration. Substitutionally doped Group V (e.g., Nb) and Group VII (e.g., Re) elements result in p-type and n-type doping, respectively[85,120]. The electrical conductivity of MoS_2 monolayers can be tuned directly through substitutional doping of Nb and Re (Fig. 3c)[121]. Similarly, the S, Se, and Te substituted with Group XV (e.g., N and P) and Group XVII (e.g., F and Cl) elements show p- and n-doping, respectively[122,123]. Controlled doping by substitution is essential for realizing functional semiconducting devices using 2D TMDs, such as transistors and p-n junctions[124–126].

Substitutional atoms can also alter the band structure of 2D TMDs. Pure 2D TMDs phases have a fixed bandgap value in the range of ~1 to ~2 eV[127]. When forming alloys by substituting the transition metal or chalcogen atoms using the atoms from the same groups in the periodic table, the bandgap of 2D TMDs can be continuously tuned[86,88,89,93,95,97]. For instance, by adjusting the composition, the bandgap of 2D $MoS_{2x}Se_{2(1-x)}$ alloy can be changed between that of pure MoS_2 (~1.85 eV) and of pure $MoSe_2$ (~1.56 eV) (Fig. 3d)[86].

The tuning of the band structure by substituting elements in 2D TMDs directly affects their optical properties. Combining 2D TMD crystal phases to form alloys normally only shifts the intrinsic PL spectrum peak position, without introducing new active luminescence centers[86,93,95]. Apart from luminescence, the tunability of the bandgap by substitution has important implications for light absorption, which plays a critical role in photovoltaics and photodetectors. The absorption spectrum of 2D TMDs can be modulated by engineering the bandgap to make use of the different regions of the solar spectrum[128]. When substituting the transition metal atoms in 2D TMDs with elements from a different group, more nuanced effects on the optical properties can be introduced[104]. Doping with rare-earth elements introduces energy levels with unique intra-4f electronic transitions in 2D TMDs, enabling the tuning of PL and electroluminescence, as well as photoabsorption from the UV to infrared region[110,111,116,118]. It is found that the electrons in the split energy levels of the Ce dopants' f orbital can bind the holes in the valence band maximum of the Ce-doped WS_2, forming optical bright excitons[117]. These excitons collide with the free A excitons when increasing the pump fluences, reducing the A excitons' lifetime.

Line defects and their effect on electrical and optical properties

Line defects are 1D structure features at which there is a discontinuity of the ordered atomic network in 2D materials. These line defects can be the boundaries between two adjacent crystalline grains with different crystal orientations (grain boundaries), the addition or removal of a semi-infinite wedge of materials (dislocations), or the physical boundaries between the structure and the air/vacuum or other mediums the 2D structure is in

(edges). The most widely studied line defects in 2D TMDs are grain boundaries and edges. In the following, the structural characteristics of grain boundaries and edges and their effect on the electrical and optical properties of 2D TMDs are discussed.

Grain boundaries and their effect on electrical and optical properties. Grain boundaries are commonly formed during the synthesis of 2D TMDs[129]. During the CVD growth of monolayer MoS_2, individual small crystals merge to form faceted tilt and mirror boundaries that are stitched together by lines of 8- and 4-membered rings with a periodic 8-4-4 pattern[130]. Boundaries formed of 5- and 7-membered rings or a string of 4-fold rings have also been commonly observed (Fig. 4a–c)[43,131,132]. At the micrometer scale, these grain boundaries follow a zigzag direction, exhibiting nanometer-scale facets (Fig. 4d, e)[130]. Both low-angle and high-angle grain boundaries exist in 2D TMDs[133,134]. There are also mirror twin boundaries where two MoS_2 crystals intersect with a relative in-plane rotation of 180° that effectively swaps the positions of Mo and S lattice sites[135–137].

In traditional 3D semiconductors, grain boundaries are considered as scattering sites for the majority carriers and degrade transport through the formation of electrostatic barriers. Such degradation is expected to be amplified in low-dimensional materials due to a reduction in Coulomb screening (Fig. 4f). A systematic electrical transport study on the effect of misorientation angle of grain boundaries reveals that charge transport in monolayer MoS_2 sensitively depends on the grain boundaries and the tilt angle between grains (Fig. 4g)[131]. In monolayer MoS_2, mirror twin boundaries slightly increase the measured in-plane electrical conductivity, whereas tilt boundaries slightly decrease the conductivity[130]. Grain boundaries can even act as electrical conduction channels in polycrystalline 2D WS_2[138].

The changes in atomic arrangement and the broken symmetry at the grain boundaries modulate the electronic band structure, which could induce exotic electronic properties at the boundaries. Gap states at low-angle grain boundaries in monolayer WSe_2 have been detected by STM[134]. Butterfly features are observed along the grain boundaries with misorientation angles of 3–6°, with the periodicity depending on the misorientation angle[134]. In single-layer MoS_2, an unexpected bandgap tunability (as large as 0.85 ± 0.05 eV) with distance from the grain boundary has been observed[139]. In twin boundaries of monolayer $MoTe_2$, a one-dimensional Peierls-type charge density wave is also directly observed[140].

Grain boundaries also actively modify the optical properties of 2D TMDs. Spatial variations in PL are attributed to the change in optical bandgap due to growth-induced thermal strain at the grain boundaries in polycrystalline $MoSe_2$[141], though it could be related to bandgap broadening at the boundaries[142]. In single-layer MoS_2, mirror twin boundaries cause strong PL quenching, whereas tilt boundaries cause strong enhancement (Fig. 4h)[130].

Edges and their effect on electrical and optical properties. Both armchair and zigzag edges can exist in 2D TMDs[143]. The zigzag edge structure consists of atoms arranged in a zigzag pattern with alternating bonds pointing in opposite directions, resulting in a high density of unpaired electrons. In contrast, the armchair edge structure has atoms arranged in a straight line, with all bonds pointing in the same direction. Zigzag edges are the most often observed edge structure in atomically thin TMDs (Fig. 5a–c)[144–146]. More complex reconstructed edge structures, such as Klein edge, have also been directly observed in atomically thin MoS_2 (Fig. 5d)[145]. The TMDs edges can be terminated by either transition metal or chalcogen atoms.

In 2D TMDs, similar to other 1D defects, the discontinuity of polarity at the edges is believed to cause metallic behavior at the edges[147]. In MoS_2, theory predicts that the zigzag edge is metallic, while the armchair edge is semiconducting[146,148,149]. Experimentally, the metallic states at the edges have been observed in single-layer MoS_2 grown on an Au substrate by using STM (Fig. 5e, f)[150]. Edge-induced band bending and electronic transition in atomically thin MoS_2 have also been found[151,152]. Using 4D STEM, atomic-scale oscillations have been detected in the electric field of a 1D edge state, with spatial variations that depend on the specific periodic edge reconstructions (Fig. 5g–i)[153]. Furthermore, edges play a critical role in establishing high-quality electrical contacts on 2D TMDs. When contact metal is deposited on the top surface of 2D TMDs, the existence of a vdW gap or Fermi level pinning by interface states results in a strong Schottky barrier at the contact. In contrast, because of the in-plane covalent bonding and metallic edge states, edge atoms strongly hybridize with metal atoms, greatly reducing the tunnel barrier and giving rise to Ohmic contacts[154–157].

The electronic structure and lattice symmetry changes at the edges of the 2D TMDs result in strong resonant nonlinear optical susceptibilities, which can be used for direct optical imaging of the atomic edges and boundaries of a 2D material[158]. In MoS_2 nanoribbons, the edge states cause a shift in PL to higher energy than that from 2D crystals[159]. A strong enhancement of PL has been found at the edge of WS_2 islands[160]. The edges of TMD monolayers also give rise to enhanced nonlinear optical properties, particularly in second-harmonic generation (SHG) (Fig. 5j–l)[158,161]. SPEs have been discovered at the edges of both monolayer and multi-layer WSe_2 flakes and have been attributed to quantum-dot structures formed at the edges[79].

Planar defects and their effect on electrical and optical properties

Lattice distortion and structural disorder can involve atoms in one or more atomic layers in 2D TMDs. We categorize these structural disorders as 2D (planar) defects. One example is lattice strain, which is ubiquitous in 2D TMDs and strongly influences their electrical and optical properties. Furthermore, when the individual atomic layers are stacked together to form 2D vdW structures, structural disorder may emerge due to the variation and inhomogeneity in layer stacking. Stacking disorder is unique to 2D vdW materials and normally doesn't exist in 3D bulk crystals. In the following, the latest development in the study of structural characteristics of stacking disorder and strain, as well as their effect on the electrical and optical properties of 2D TMDs, is discussed.

Stacking disorder and its effect on electrical and optical properties. The stacking and alignment between the constituting atomic layers in 2D materials are characterized by the relative twist and in-plane displacement between the layers. In both 2D homostructures and heterostructures, the stacking disorder of atomic layers is ubiquitous due to the local variation and inhomogeneity in the alignment and registry between the adjacent atomic lattices, as well as lattice relaxation[50,162–165]. It constitutes a type of disorder not found in conventional materials. Stacking disorder in in-plane shift/sliding between the individual atomic layers has been directly observed in pristine exfoliated $MoTe_2$ thin flakes (Fig. 6a, b)[166]. $MoTe_2$ nanoflakes show highly disordered stacking, with nanoscale 1T' and T_d domains, as well as alternative stacking arrangements with in-plane displacement not found in the bulk (Fig. 6a, b)[166]. In twisted bilayer or multilayer TMDs, the twist angle between the atomic layers is often inhomogeneous at the nanometer scale, which can distort the local moiré lattice (Fig. 6c)[47,48,50,163,167]. In addition, the interaction between atoms in the adjacent atomic layers could cause lattice relaxation in TMD homobilayers and heterobilayers, resulting in domain structure and strain (Fig. 6c)[47,48,168–170].

The electrical and optical properties of 2D vdW structures sensitively depend on the stacking of the atomic layers. In homostructures, the disorder in the in-plane shift between the atomic layers effectively changes structural phases in the original lattice, resulting in a large variation of the electrical and optical properties within the 2D TMDs. In twisted homo- and heterobilayers of the TMDs, MoS_2 and WS_2, STM measurements show that lattice reconstruction creates strong piezoelectric textures[48]. The variations in valence and conduction band edges due to non-uniform moiré lattice in twisted heterobilayer $WSe_2/MoSe_2$ have been observed (Fig. 6d–f)[50]. Moreover, the indirect bandgap size varies appreciably with the stacking configuration. Reconstruction of moiré patterns in twisted WSe_2/WSe_2 as

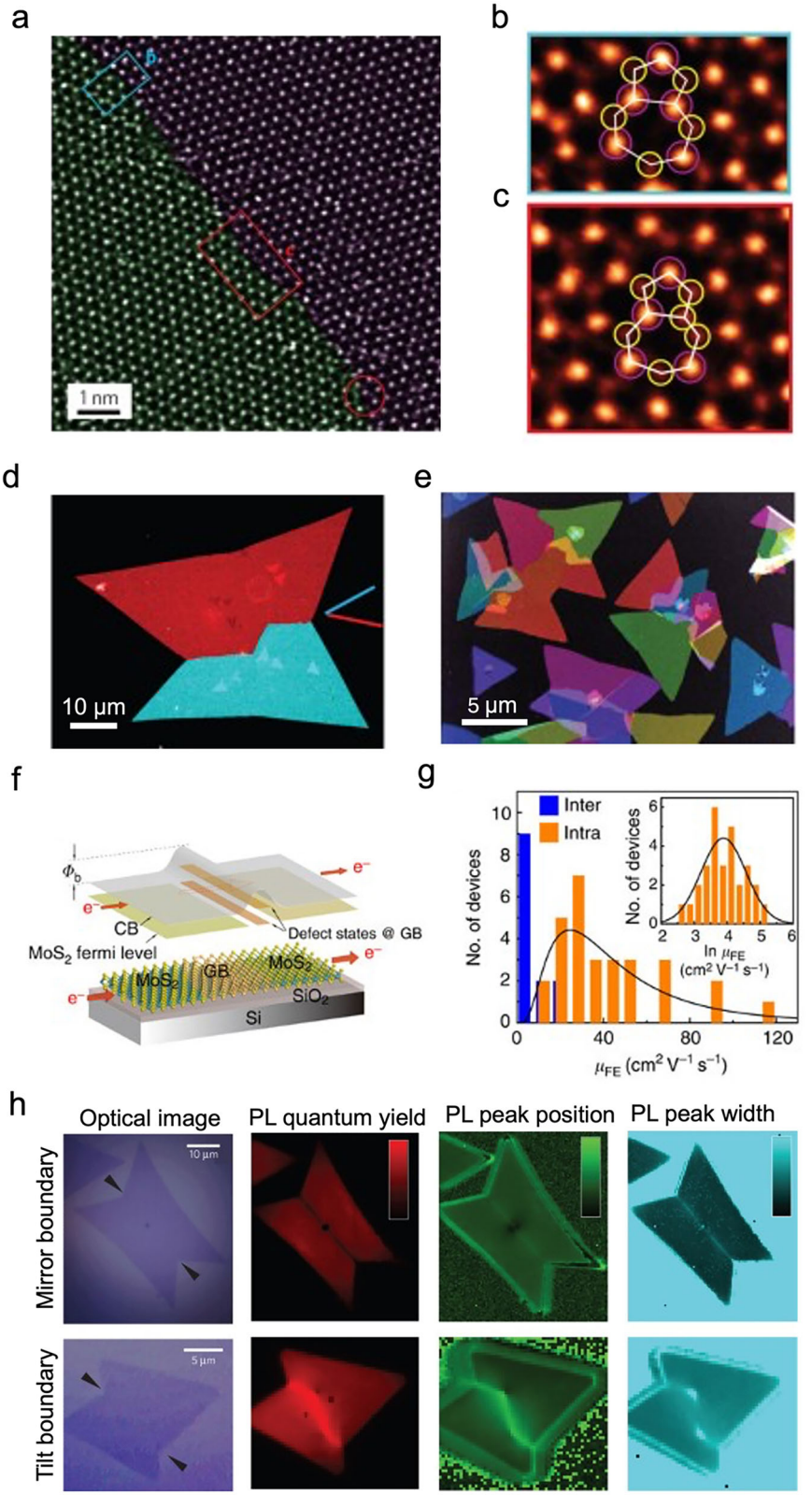

Fig. 4 | Grain boundaries in 2D TMDs. a STEM ADF image of a MoS_2 grain boundary with false color depicting the grains on both sides of the boundary[132]. **b**, **c** Zoom-in images of the regions highlighted in (**a**). The purple circles are Mo, and the yellow ones are S_2 columns[132]. **d** Color-coded TEM dark field (DF) image shows a tilt grain boundary as a faceted line connecting the two triangles[130]. **e** Color-coded TEM DF image shows multiple polycrystalline monolayer MoS_2 flakes with varied grain sizes. The grains are all connected by faceted, abrupt grain boundaries[130]. **f** Schematic of carrier transport across a grain boundary in monolayer MoS_2, where there is a potential barrier for electrons[131]. **g** Statistical distribution of the intra- and inter-grain mobilities with $\mu_{FE}(inter) < 16\ cm^2\ V^{-1}\ s^{-1} < \mu_{FE}(intra)$[131]. **h** Optical measurements of a monolayer MoS_2 island containing a mirror twin boundary and an island containing a tilt boundary. In PL quantum yield, there is a 50% quenching at the mirror twin boundary and a 100% enhancement at the tilt boundary. For the peak position, there is an upshift of 8 meV at the mirror twin boundary, and a much stronger 26 meV upshift in the tilt boundary. The peak broadens from 55 to 62 meV at the boundary in both samples[130].

well as $MoSe_2/MoSe_2$ bilayers results in variation in moiré periodicity and symmetry, which is correlated with the emergence of new exciton species (Fig. 6g, h)[165,168,171].

Stacking disorder in 2D TMDs has often been overlooked, though it strongly affects their electrical and optical properties. The characterization of stacking disorder at the nanometer and atomic scales is still rudimentary and needs to be further established using advanced microscopy techniques. A detailed and comprehensive investigation of local stacking disorder on the electrical and optical properties of 2D TMDs is critical for the further development of TMD vdW structures.

Strain and its effect on electrical and optical properties. Strain is another type of structure imperfection commonly found in 2D TMDs and can be used to actively tune their electrical and optical

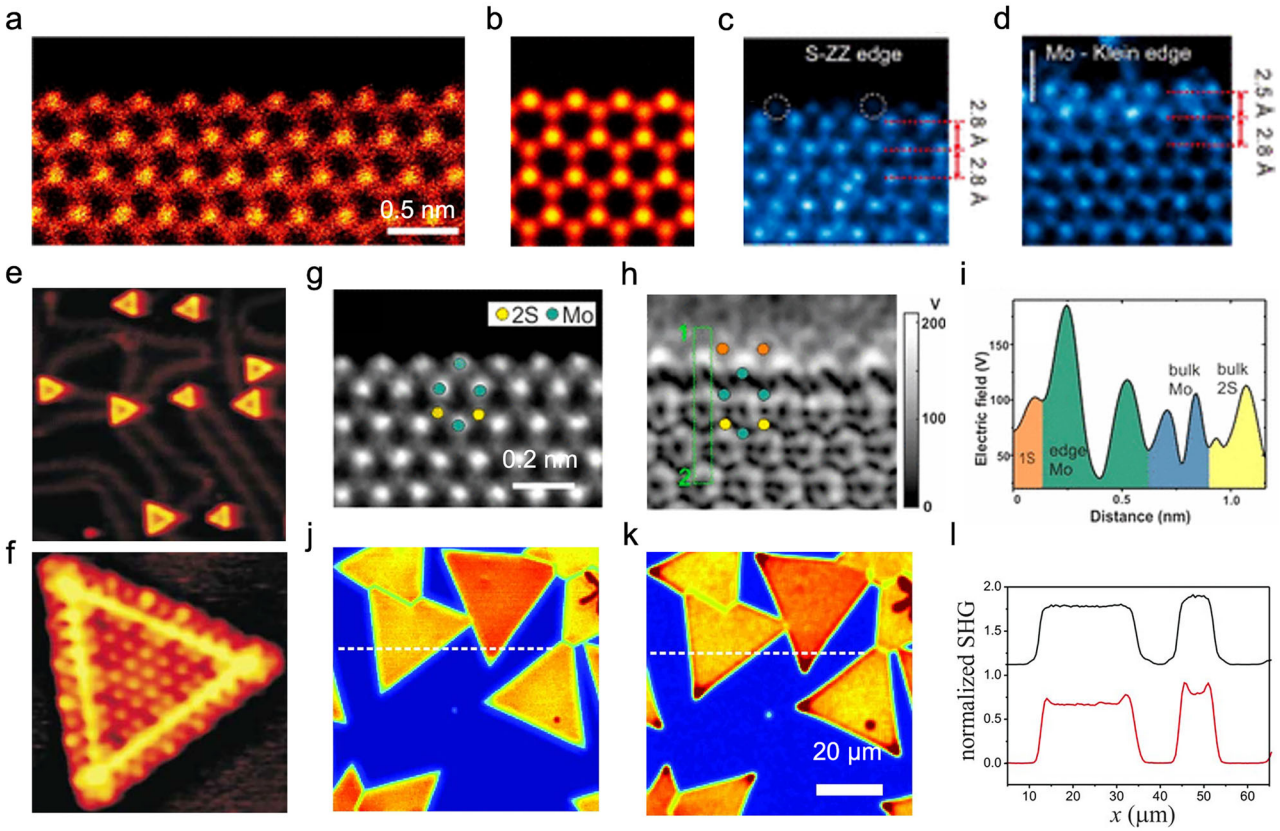

Fig. 5 | Edges in 2D TMDs. a Atomic resolution STEM ADF image of a Mo-terminated zigzag edge in monolayer MoS_2[144]. **b** Simulated STEM ADF image at the zigzag edge[144]. **c** Atomic resolution STEM ADF image of a S-terminated zigzag edge[145]. **d** STEM ADF image of a Mo-terminated Klein edge. Changes in lattice distance are labeled[145]. **e** STM image (278 × 282 Å^2) showing triangular MoS_2 nanoclusters dispersed on a reconstructed Au(111) surface[150]. **f** Single MoS_2 nanocluster (48 × 53 Å^2). The nanoclusters show a brim of very high conductance extending all the way around the edge, giving rise to metallic edge states[150]. **g**, **h** STEM ADF image showing the Mo reconstructed zigzag edge structure and the corresponding projected electric field map calculated from a 4D-STEM data set[153]. S and Mo atoms are indicated by yellow and green markers, respectively. **i** Intensity line profiles of the area marked by a box in (**h**), color-coded for different atoms. The twin peaks indicate the splitting of the electric field on opposite sides of the atom. Variation of the electric field at the edge at the atomic scale is visible[153]. **j** Secondary harmonic generation (SHG) image pumped at 1280 nm[158]. **k** SHG image of the same sample pumped at 1300 nm[158]. The brim of crystal shows a strong nonlinear optical (SHG) edge state. **l** Profile of SHG signal (white dashed lines in **j**, **k**) compares the SHG of the same crystals under pump wavelengths of 1280 nm (black) and 1300 nm (red), respectively. The enhanced edge responses are clearly shown[158].

properties[172–175]. The intrinsic lattice defects, such as point defects and line defects, can result in localized lattice distortion and strain surrounding the structural defects (Fig. 7a–h)[176–178]. Strain can also be applied to the 2D TMDs externally. The ultimately small thickness and the large degree of freedom in the out-of-plane direction of 2D TMDs make them easy to deform and buckle. The high crystalline quality and strong in-plane covalent bonding between the atoms allow atomically thin 2D TMDs to withstand large strain[179,180].

Different types of strain, including uniaxial, biaxial, and hydrostatic strain, as well as bending, buckling, and rippling, can be introduced in 2D TMDS[172]. Though the fracture strain of a monolayer MoS_2 membrane is demonstrated to be around 10%[181], the magnitude of the highest strain that has been realized in 2D TMDs is usually around 2–3%. The theoretical strain limit of atomically thin TMDs is expected to be around 20%[179,180].

Strain changes the lattice symmetry, bond length, and angle, profoundly affecting the bonding and electronic band structure in 2D TMDs. Strain can cause the shift, split, and warp of the conduction and valence bands in semiconductors[45,182–188], and modify charge distribution and electronic states close to the Fermi level. Strain induces an indirect to direct bandgap transition in few-layer WSe_2 with a uniaxial tensile strain up to 2%[187]. The optical bandgap of MoS_2 decreases approximately linearly with strain, ~45 meV/% strain for monolayer MoS_2 and ~120 meV/% strain for bilayer MoS_2 (Fig. 7i, j)[188]. Moreover, strain-induced changes in resistivity and charge mobility have also attracted interest[184,189–191]. Interestingly, the carrier mobility in 2D MoS_2 can be improved with rippled materials[192]. The mechanical properties and the strong tunability of the electronic properties by strain of 2D TMDs hold great promise for realizing 2D straintronics[127].

Lattice strain impacts the optical properties of 2D TMDs. The change of bandgap by mechanical strain directly results in a continuously tunable PL signal[188,193–197]. A bandgap modulation of 0.2 eV is believed to be the origin of strain-engineered high-responsivity $MoTe_2$ photodetectors, which are otherwise photo-inactive without strain[198]. Dark and localized excitons in monolayer WSe_2 are brought into energetic resonance by strain, forming a new hybrid state[199]. Quantum emitters, including SPEs, have been created by localized strain in WSe_2 and WS_2 monolayers (Fig. 7k, l)[81,200,201]. SHG sensitively depends on the crystal symmetry and dielectric function of the material system, which are affected by strain. More than an order of magnitude enhancement in SHG intensity is observed from high-quality $MoSe_2$ monolayers by controlled biaxial strain[202].

Control of structural disorder

Controlling the type, density, and distribution of the aforementioned structural disorder and defects in 2D TMDs is essential for understanding their effects on electrical and optical properties and for realizing functional devices by exploiting the unique properties of the defects. The defects can be produced and controlled during the fabrication and growth of the 2D TMDs, but can also be introduced by post-fabrication methods.

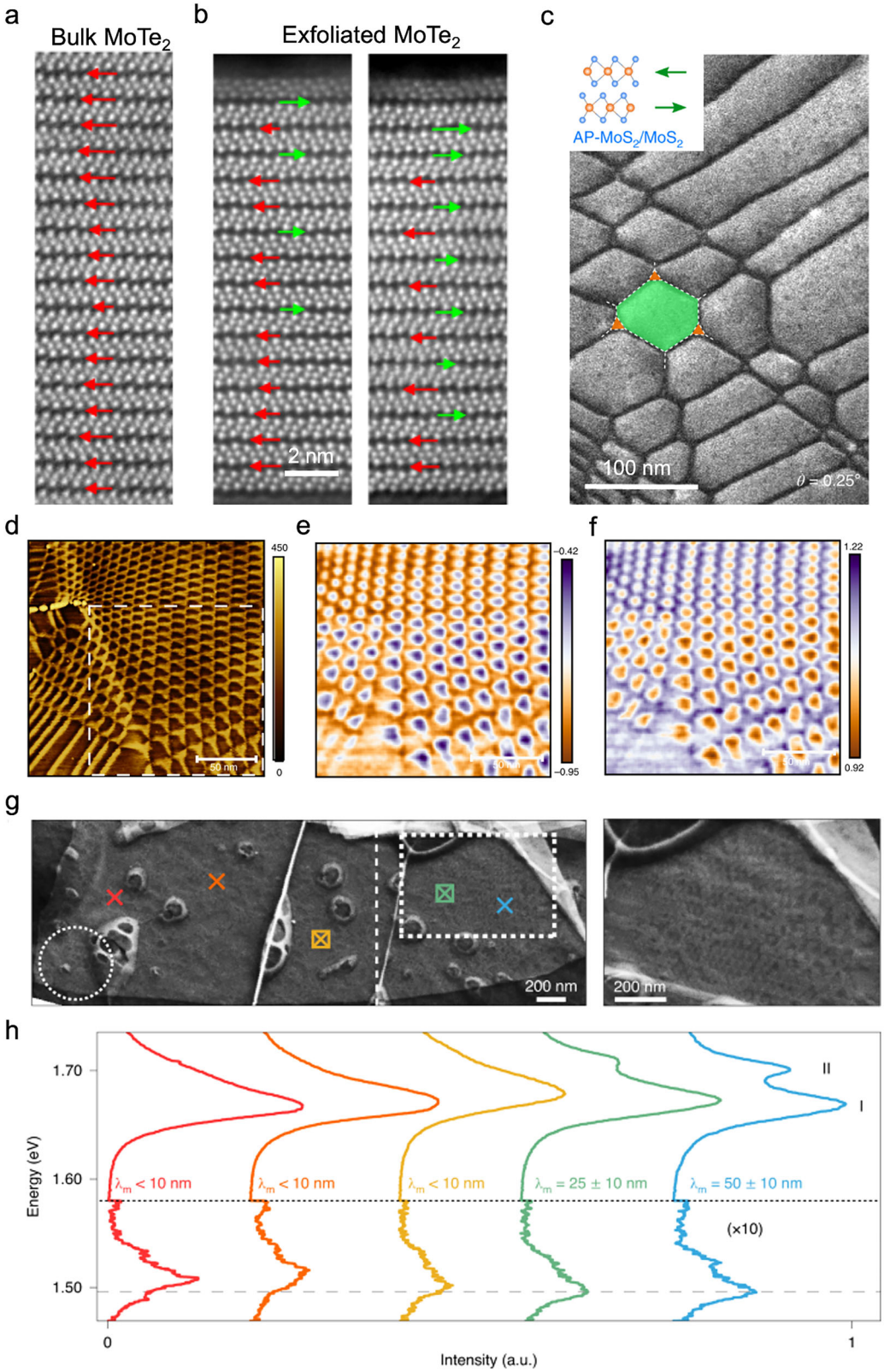

Defect engineering and manipulation have been extensively explored in bulk and nanoscale semiconducting materials and devices to achieve tailored or enhanced properties. The traditionally adopted defect engineering techniques include in situ substitution[203], high temperature thermal annealing[204], ion implantation[204,205], chemical passivation[205], and strain engineering[206], just to name a few. These strategies and methods have been applied for controlling structural disorder and defects in 2D TMDs, but the material response and effect in 2D TMDs are often quite different compared to traditional semiconductors due to the 2D morphology and ultimately small thicknesses of the 2D TMDs. For example, thermal annealing is often used to reduce point defects in traditional semiconductors[204], while annealing is commonly found to create chalcogen vacancies in 2D TMDs[207].

Fig. 6 | Stacking disorder in 2D TMD vdW structures. a Cross-sectional STEM ADF image of bulk $MoTe_2$, with overlaid arrows indicating the inter-layer shift[166]. **b** Cross-sectional STEM ADF images of a $MoTe_2$ flake exfoliated onto amorphous SiO_2 with a protective carbon overlayer[166]. The scale bar is applied to all images in (**a**, **b**). **c** Low-magnification STEM ADF image of patterns of domain structure in MoS_2 homobilayers with a nominal twist angle of 0.25°, showing the inhomogeneity in twist stacking order[48]. The inset atomic schematic illustrates the antiparallel (AP) orientation of the atomic layers, disregarding the local stacking configuration. Colors highlight different types of domains. **d** STM topograph (in pm) of a non-uniform moiré region in twisted heterobilayer $WSe_2/MoSe_2$[50]. Valence (**e**) and conduction (**f**) band edge maps (in eV) obtained from the area marked by the dashed box shown in (**d**)[50]. **g** SEM image of WSe_2/WSe_2 homobilayers showing a reconstructed moiré pattern. The moiré wavelength λ_m increases from <10 to 60 nm from left to right. The moiré pattern is not visible left of the vertical dashed line. The dashed circle indicates the optical beam spot size, and the crosses indicate the beam spot centers for PL measurements[168]. **h** PL spectra collected from the locations marked with crosses in (**g**). The spectra are offset for clarity, and the intensity is multiplied by 10 below 1.58 eV. The higher-energy exciton peak emerges with increasing λ_m, and the interlayer exciton emission is blue-shifted for $\lambda_m < 10$ nm[168].

The 2D morphology also demands tailored and novel methods for controlling structural disorder in 2D TMDs.

In this section, some widely utilized techniques that show promise in effectively and efficiently controlling structural disorder in 2D TMDs will be discussed. Structural disorder can be introduced and controlled both during material fabrication and after fabrication. Techniques for controlling structural disorder during material fabrication and growth are first described. In situ engineering of point defects, control of grain boundaries and edges, as well as introducing lattice strain by substrates during fabrication, are discussed. Then, advances in post-fabrication engineering of structural disorder are reviewed. Important and promising techniques that are discussed include externally applied strain/stress, irradiation and implantation using charged particles, photon illumination, and electric field manipulation, as well as mechanical stacking.

Disorder control during material fabrication

In situ control of point defects. A range of thin film growth techniques, such as PVD, vapor phase transport, CVD, molecular assembly, atomic layer deposition, etc., have been applied to grow atomically thin TMDs. CVD is one of the most widely used techniques to realize controlled growth of 2D TMDs[208,209]. The CVD approach has demonstrated great potential in the synthesis of high-quality TMD monolayers, due to its excellent controllability and scalability (Fig. 1j)[132,210,211,212]. The growth temperature, gas flow, precursor, and substrate all affect the resulting atomic layers and can be used to tune the crystallinity, grain size, stoichiometry, type, and density of defects in 2D TMDs[210,213].

A common way of doping and forming alloys in 2D TMDs is to introduce a dopant precursor into a CVD system during material growth[97,214]. Examples are alloy $MoS_{2x}Se_{2(1-x)}$ triangular nanosheets with complete composition tunability[86] and "in situ" transition-metal (such as Nb and Re) substitution doping in TMD monolayers[101,121]. Doping with rare-earth elements in 2D TMDs has also been frequently realized by CVD growth[111,116]. The complete composition $MoS_{2x}Se_{2(1-x)}$ nanosheets were synthesized through a tailored CVD route, where a temperature gradient was applied for the composition selection. An alumina boat loaded with MoO_3 powder was placed into the heating zone of a quartz tube, and another two boats loaded with sulfur and selenium powder were placed at the upstream. Several pieces of Si substrates (with 300 nm SiO_2) were placed on the alumina boat with MoO_3 powder. The furnace was rapidly heated to 830 °C and maintained at this temperature for 8 min, keeping the pressure inside the tube at 8 Torr. $MoS_{2x}Se_{2(1-x)}$ nanosheets with gradually changed composition were deposited on different positions of SiO_2 surfaces along the length of the tube[86]. For introducing and controlling substitutional dopants such as Nb and Re, $NbCl_5$ and $Re_2(CO)_{10}$ were used as precursors that were introduced into the reactor in the gas phase in a CVD process. The flow rates were precisely regulated using Ar carrier gas and temperature control. The flow rates are 0.1 sccm for $Mo(CO)_6$, 0.3 sccm for $C_4H_{10}S$, 1 sccm for H_2, and 800 sccm for Ar. The growth was performed at 750 °C for 4 h. In this manner, continuous MoS_2 monolayers were synthesized over the entire substrate, where the concentration of Nb or Re was reproducibly tuned over a wide range up to 20%[121].

The dominant point defects in CVD-grown TMDCs are the chalcogen vacancies, with densities on the order of 10^{12}–10^{13} cm^{-2}[61,215,216]. Alternative precursors such as sulfur-containing thiol solution and hydroxide W species have been employed to provide an energetically favorable route for the chalcogenization process in the TMDC growth, reducing the defect density by approximately an order of magnitude[217,218]. In addition, a chalcogen monomer supply method has been developed as a defect-healing strategy to achieve stoichiometric TMD films[219].

Engineering grain boundaries and edges during growth and fabrication. The CVD approach has shown promise for TMD edge engineering (1H, 1T or 1T'-zigzag or armchair edges) as well as achieving diverse edge morphologies (1D nanoribbons, 2D dendrites, 3D spirals, etc.)[143]. For example, a universal route for synthesizing arrays of unidirectionally orientated monolayer TMDs ribbons (e.g., MoS_2, WS_2, $MoSe_2$, WSe_2, MoS_xSe_{2-x}), by using the step edges of high-miller-index Au facets as templates, has been demonstrated[220]. Synthesis of MoS_2 on Si(001) surfaces pre-treated with phosphine yields high-aspect-ratio nanoribbons of uniform width[159]. By adding minor H_2 carrier gas in Ar, the shape of monolayer WS_2 flakes can be controlled from jagged to straight edge triangles[221]. Grain boundaries and twin boundaries are also commonly present in CVD-grown 2D TMDs and can be controlled by growth parameters such as gas flow, temperature, and substrate[130,133,222].

The weak interlayer vdW bonding enables the fabrication of atomically thin 2D TMDs by mechanically exfoliating bulk crystals[22]. Micromechanical exfoliation of TMDs single crystals, using the so-called "scotch tape" method, is still one of the most popular methods that produce 2D TMDs with a high degree of crystallinity and cleanness[3,16,22,223]. The exfoliation results in flakes with varied thickness and size. Atomically thin flakes produced this way are usually relatively small, with a size in the range of a few to tens of μm^2. A more recent variation of the method, Au-assisted mechanical exfoliation, can produce monolayer TMDs with a size up to a centimeter scale[224–228].

The defects and structural disorder, such as vacancies, dopants, and grain boundaries, in mechanically exfoliated 2D TMDs are inherited from the original bulk crystals. Normally, when natural or synthesized single crystals are used, the most common defects are chalcogen vacancies. The exfoliation process results in the breaking of the atomic layers along the principal crystallographic directions[42,67]. The resulting edges of TMD flakes are expected to be terminated with either armchair or zigzag edges. The type and distribution of the edge are more difficult to control during mechanical exfoliation. Patterning by chemical etching of the exfoliated flakes has been demonstrated to be capable of precisely creating and controlling edge size and orientation in exfoliated 2D TMDs[229]. In this process, TMDs can be etched along certain crystallographic axes, and the obtained edges are nearly atomically sharp and exclusively zigzag-terminated.

Substrate-induced strain. The atomically thin 2D TMDs often need to be grown on or transferred to dedicated target substrates to be characterized and studied, or to be integrated in device fabrication. The substrate that supports the thin flakes can induce strain in 2D TMDs, either intentionally or unintentionally.

SiO_2 on Si is the most used substrate for investigating 2D TMDs. When transferring monolayer or few-layer TMDs on SiO_2, ripples or bending are often induced in the layers due to surface corrugation on the substrate surface. A large bandgap modulation of 1.23–2.65 eV in monolayer MoS_2 on

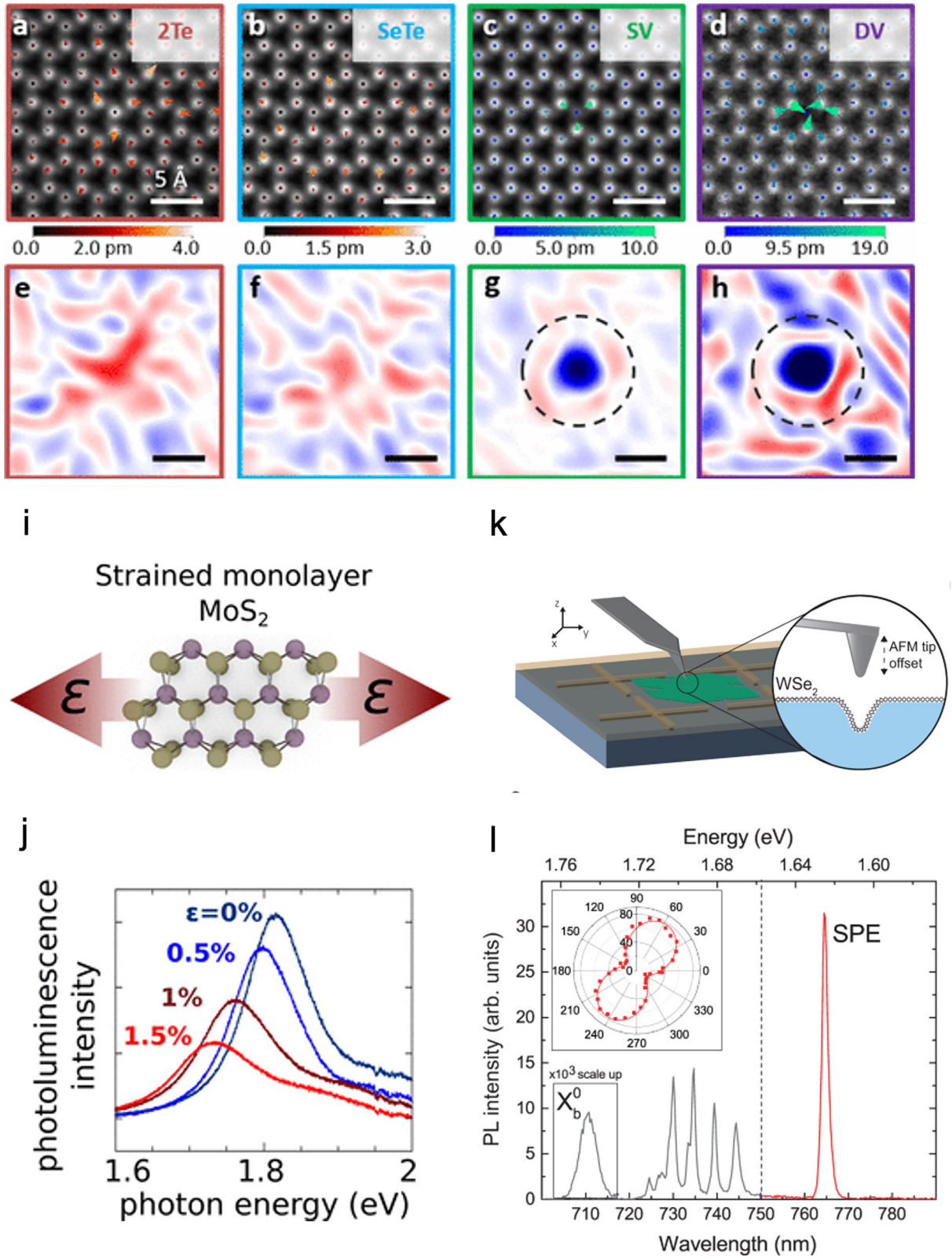

Fig. 7 | Strain in 2D TMDs. a–d STEM ADF images of point defects at chalcogen sites in monolayer $WSe_{2-2x}Te_{2x}$ with two-dimensional displacement vector field overlaid. The vectors are enlarged for visibility[176]. **e–h** Experimental dilation fields calculated from the displacement fields. The dilation corresponds to the local projected area change. Double substitutions (2Te) and single substitution (SeTe) exhibit local expansion, while single vacancy (V_s) and double vacancies (DV) exhibit local contraction[176]. The scale bar is the same in (**a–h**). **i** Schematic showing strained monolayer MoS_2[188]. **j** PL spectra showing the bandgap of monolayer MoS_2 shifts as a function of applied strain[188]. **k** Schematic of SPE fabrication by nanoindentation in a WSe_2 monolayer transferred onto a substrate with an alignment pattern[200]. **l** PL spectrum from a selected SPE. The spectral part detected in the experiment is highlighted in red color. Spectral peak of the free bright neutral exciton X_b^0 at $\lambda = 710.5$ nm is scaled up by 10^3. The inset a shows typical polarization-resolved spectrally integrated PL signal from an SPE[200].

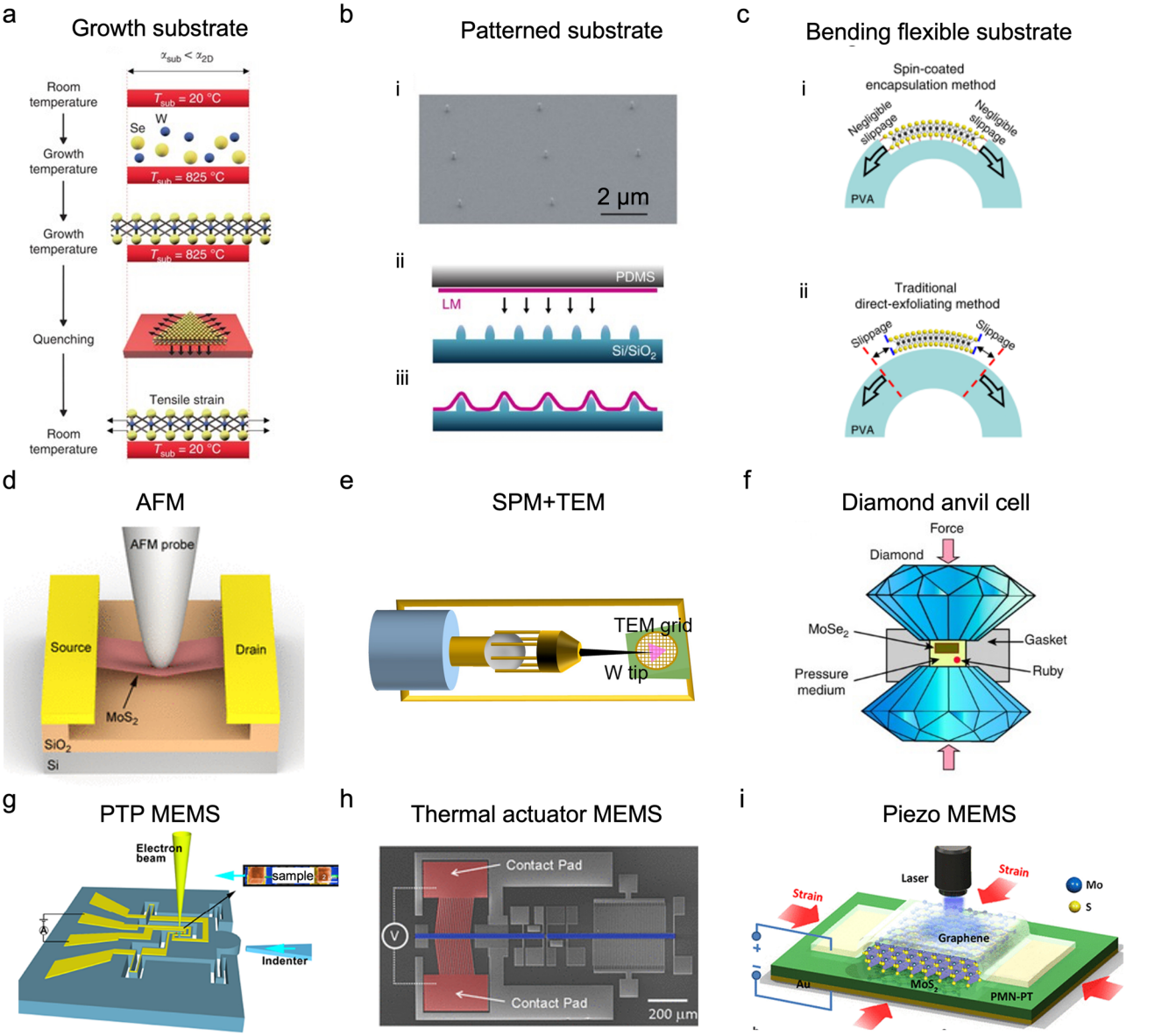

Fig. 8 | Techniques for strain engineering of 2D TMDs. a The difference in thermal expansion of the 2D TMDs and their growth substrate causes strain during CVD growth of 2D TMDs[292]. **b** Patterned substrate used to induce strain in 2D TMDs: i SEM image of a SiO_2 substrate fabricated with nanopillars on the surface. ii Schematic of the transfer of a 2D TMD layer onto the substrate. iii Schematic showing that the transferred 2D TMD is strained by the nanopillars[81]. **c** Strain introduced by bending a flexible substrate that the 2D TMDs are attached to: i Strain transfer improved by anchoring the 2D flake by a spin-coated polymer. ii Conventional approach with significant slippage[239]. **d** AFM probe for introducing local strain[184]. **e** SPM-TEM setup for in situ straining 2D TMDs in TEM[247]. **f** Diamond anvil cell for applying high (up to 100 GPa) hydrostatic pressure on 2D TMDs[251]. **g** Push-to-pull microelectromechanical system (MEMS) device for applying uniaxial tensile strain[257]. **h** Thermal actuator-based MEMS for applying uniaxial strain[293]. **i** Piezo device for applying uniaxial or biaxial strain on 2D TMDs[258].

a SiO_2/Si substrate has been found, due to the inherent local bending strain induced by the surface roughness of the substrate[45]. Atomically flat substrates, such as graphite or hBN, are thus often used to diminish substrate-induced strain for high-quality device fabrication of 2D TMDs. However, it has been observed that tensile strains in bilayer and trilayer MoS_2 can also be caused by the typical experimental process of hBN encapsulation[230]. Intrinsic strain and structure heterogeneity have also been observed in MoS_2 atomic layers grown by CVD on SiO_2 substrates[222]. Controlled biaxial tensile strain up to 3% in $MoSe_2$ monolayers can be created by substrates in PVD synthesis[202]. Such substrate-induced strain originates from the difference in thermal expansion between 2D TMDs and the substrate during the cooling process after high-temperature growth (Fig. 8a).

Various target substrates have been adopted to introduce and control strain in 2D TMD flakes, making use of the property that 2D flakes are usually attached strongly to the substrates and follow the morphology of the substrate surface. Flexible substrates are frequently utilized for this purpose. Local strain up to 2.5% is introduced in MoS_2 and WSe_2 flakes due to wrinkles created by pre-stretching and releasing an elastomeric substrate[194,231]. Substrates with prefabricated patterned surface structures have also been used to control localized strain in atomically thin TMDs (Fig. 8b)[192]. SPE arrays have been demonstrated in monolayer WSe_2 transferred onto substrates with pre-patterned dielectric nanopillar structures[81,82,232]. Substrate-directed strain is also observed in bilayer MoS_2 on amorphous holey silicon nitride substrates, which are widely used for TEM study of 2D materials[233].

Post-fabrication control of structural disorder

Externally applied strain/stress. Lattice strain cannot only be introduced during the growth and fabrication of 2D TMDs, but can also be

applied externally. The most straightforward way to apply in-plane strain in 2D materials may come from transferring them on a flexible substrate and directly stretching, compressing, or bending the substrate (Fig. 8c)[173,188,189,196,197,234]. Such an approach is versatile. Polymer substrates such as Polydimethylsiloxane (PDMS) and Polypropylene (PP) have been commonly used[235]. The deformation of the substrates can be controlled by mechanical or heating actuators[195,235–238]. However, there can be significant slippage of the 2D flakes on the substrates during the stretching or bending of the substrates, if the 2D flakes are not anchored[239]. As a result, the strain introduced in the 2D materials in many studies could be overestimated (Fig. 8c). Clamping of the 2D atomic layers on the flexible substrates has been achieved using techniques like metal contact fabrication and polymer encapsulation (Fig. 8c)[240].

Nanoprobe-enabled straining has also been used as an effective way of creating precisely controlled strain in 2D TMDs. A sharp tip in a SPM, such as an atomic force microscope (AFM), can be used to indent an atomically thin TMD membrane (Fig. 8d)[181,184,241–243]. A unique design that integrates an SPM in a TEM or SEM sample holder can also be used for studying strain-induced effects (Fig. 8e)[244–246]. Such a setup allows a combined and simultaneous measurement of structural response at high spatial resolution and electrical/optical characteristics of nanomaterials, providing unique information on strain and stress-induced effects in 2D TMDs. The setup has been used to investigate atomic-scale structural evolution in 2D materials under stress in TEM[247,248]. It has also been utilized to investigate strain-induced structural as well as optical and electrical response of 2D TMDs[249]. Shear-stress-induced interlayer sliding, as well as atomic layer cleavage and bending in MoS_2, has been introduced using the nanoprobe in the setup and observed in the cross-section view in situ in a TEM[250].

Hydrostatic compression through a diamond anvil cell (DAC) has been applied to study the effect of high pressure on 2D TMDs (Fig. 8f)[251–256]. The DAC can produce a pressure (>100 GPa) that is orders of magnitude higher than other commonly used stressing techniques. It is found that interlayer interaction in 2H-stacked WSe_2-$MoSe_2$ heterostructures can be effectively tuned by hydrostatic pressure. An evolution and transition of interlayer excitons in WSe_2-$MoSe_2$ heterostructures with a pressure-induced band changeover has been observed[252].

Microelectromechanical systems (MEMS) devices have been utilized to induce and control strain in a wide variety of nanomaterials, including 2D materials (Fig. 8g–i)[182,257–260]. These MEMS straining devices have appealing advantages such as high precision, high controllability, stable and small footprint, but the application of the MEMS devices to study strain introduced changes in lattice structure and physical properties of 2D TMDs has not been extensively explored yet. One challenge is the reliable and efficient transfer of ultrathin 2D TMDs onto specific locations on the devices[261].

Irradiation and implantation. Irradiation and implantation using energetic charged particles, including electrons and ions, are an effective way to create and control defects in 2D TMDs after their fabrication. The high resolution and precision of this approach make it attractive.

An electron beam with an energy in the range from tens of keV to a few hundred keV can create defects in atomically thin TMDs. One of the most common defect-generation processes in the interaction between a high-energy electron beam and 2D lattices is knock-on damage[262,263]. Defects created in 2D TMDs have been commonly observed and extensively studied in TEM (Fig. 9a)[262–264]. The typical beam energy in a TEM (tens to a few hundred keV) is high enough to create defects in 2D TMDs, and modern TEMs with aberration correctors have sub-Å spatial resolution, making them ideal tools to directly observe and quantitatively study electron beam-created defects in 2D TMDs. The most common defects generated by electron beam illumination are chalcogen vacancies, which have much lower knock-on threshold energies than the transition metal atoms (Fig. 9a)[262,263,265]. Vacancies generated by high-energy electron beam have been found to facilitate phase transitions in ReS_2[266]. SPEs in monolayer WSe_2 have been created by electron beam illumination[82]. Atomically thin TMDs can also be sculptured, creating nanoscale structures such as ribbons, wires, and pores, using a focused electron beam in TEM[267]. Energetic ion beams, such as helium ion and gallium ion beams, can also sputter atoms in 2D TMDs, creating vacancies (Fig. 9b, c)[268].

Plasma treatment is a mature surface modification and doping technology in silicon-based semiconductor processes. It can be utilized for precise regulation of carrier type and concentration, band structure, and contact of 2D TMDs[71,269,270]. Both cationic and anionic elements can be replaced by external impurity atoms during plasma modification[271–276]. For instance, N plasma was used to heal the S vacancies in 2D WS_2 (Fig. 9d)[277].

Controlling structural disorder using light and electric field. Photon and electric field can also be utilized to generate defects, as well as modify atomic structure and stacking order in 2D TMDs.

It is demonstrated that ultraviolet photons in vacuum generate vacancies in MoS_2 monolayers, exhibiting single-photon-emitter characteristics, whereas those created in air lack quantum emission attributes due to oxygen passivation[278]. The reversible photo-induced doping of few-layer $MoTe_2$ and WSe_2 has been reported[279]. The 2D TMD channel polarity can be reconfigured from n-type to p-type, and vice versa, with laser light at different frequencies. This reconfigurable doping is attributed to selective light-lattice interactions, such as the formation of Te self-interstitial defects under ultraviolet illumination and the incorporation of substitutional oxygen in Te and Mo vacancies under visible illumination (Fig. 10a–f)[279]. Laser irradiation can also generate chalcogen defects in 2D TMDs. For instance, laser irradiation introduces Te vacancies, which trigger the phase transformation from 2H to 1T phase in $MoTe_2$ (Fig. 10g)[280]. The elevated temperature by laser irradiation (400 °C) is the main factor that generates Te vacancies. While the structure change in $MoTe_2$ caused by laser is irreversible, light-induced reversible phase transition has been observed in mono- and bilayer ReS_2[266]. In addition, lasers have been used to locally etch 2D TMDs, creating edges[281].

An electric field can be used to tune the electronic and crystalline structure of 2D TMDs. Structural phase transition in monolayer $MoTe_2$ driven by electrostatic doping via an ionic liquid has been observed[282]. Atomic-scale structure modification and novel structural phases in $MoTe_2$ and $Mo_{1-x}W_xTe_2$ induced by a static electric field have been reported[283]. An out-of-plane electric field can cause the rearrangement of moiré domains and tune stacking disorder in twisted bilayer WSe_2, as revealed by an in situ TEM investigation (Fig. 10h–k)[284]. The tuning effect originates from the interaction between the electric field and the ferroelectric domains in the 2D stacks.

Structural disorder via mechanical transfer. Mechanical transfer can also introduce structural disorder in 2D TMDs. The exfoliated and as-grown atomically thin TMD flakes or films often need to be transferred to a target substrate for characterization and device fabrication[272,273,285]. Mechanical transfer and stacking have been among the most popular ways to transfer the TMD atomic layers, as the method largely maintains the pristine structure and intrinsic properties of 2D TMDs (Fig. 11a)[274,275,285]. Moreover, artificial 2D TMDs heterostructures are predominantly produced by mechanical transfer and stacking due to the relatively high degree of controllability and precision of the methods[40,47,48,163].

Mechanical transfer could induce strain, as well as ripples and folds in 2D TMDs. Moreover, stacking disorder in 2D vdW structures predominantly originates from the mechanical transfer process[40,47,48,163]. Such disorder has a strong impact on the reproducibility of the 2D vdW structures[163,275,276]. The fabrication of the 2D heterostructures often remains a manual process, making the structures prone to stacking disorder. Any variations in in-plane sliding and twist between the atomic layers during transfer will cause stacking disorder at the nanometer and atomic scales. The fabrication of homogeneous and highly reproducible devices remains a big challenge and the main limiting factor of the advancement of the field of 2D vdW heterostructures. Although progress has been made towards reducing or controlling stacking inhomogeneity, for example, by the standardization

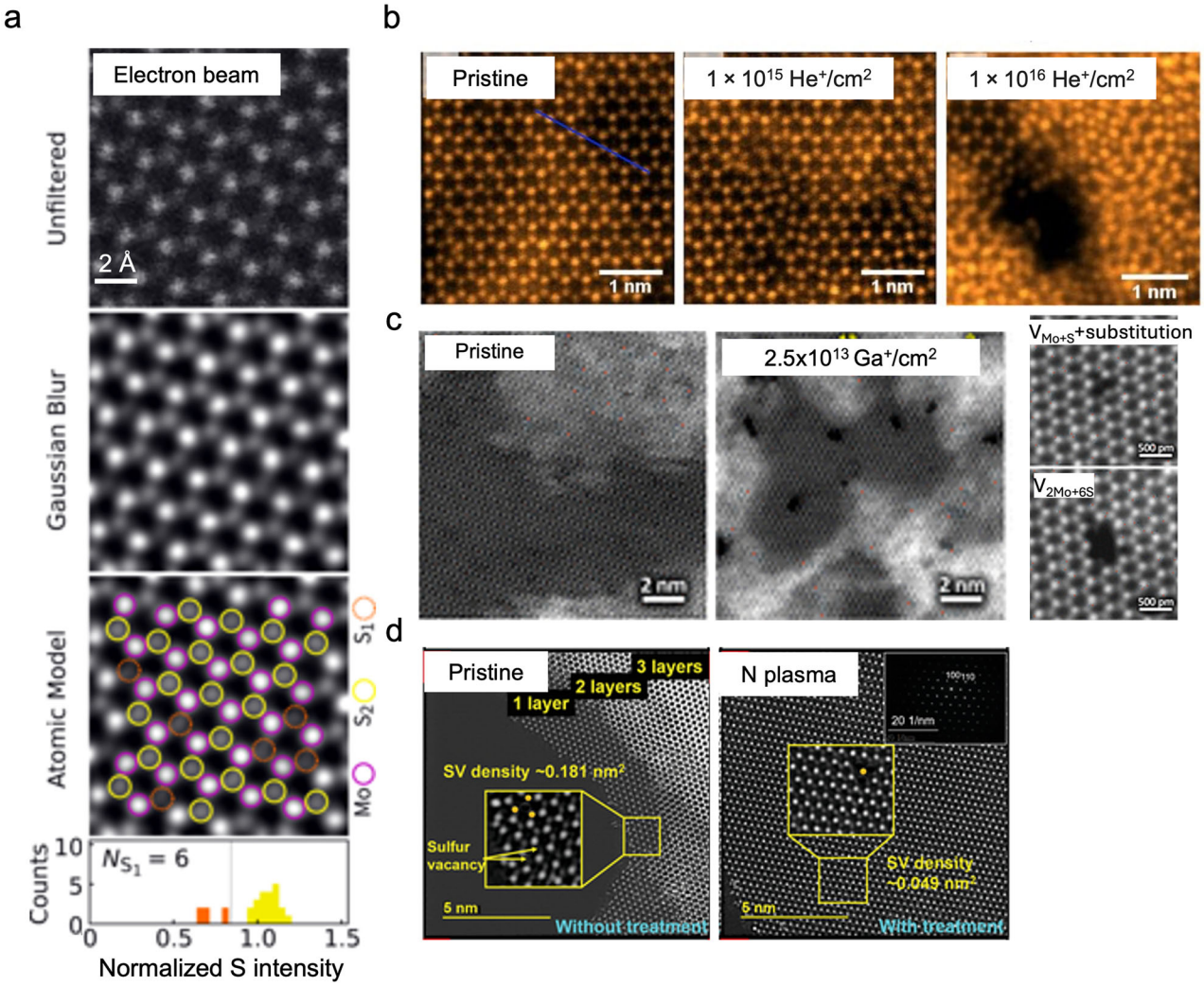

Fig. 9 | Irradiation for controlling defects in 2D TMDs. a The effect of a high-energy electron beam. From top to bottom: as-recorded STEM ADF image of monolayer MoS_2, Gaussian-blurred image of the as-recorded STEM image, an atomic model overlayed on the image indicating the positions of the atomic sites (solid purple circles indicate Mo atoms while solid yellow and dotted orange circles highlight a column of two S atoms and a single S atom/single S vacancy, respectively.), histogram showing the corresponding S site intensities and the number of single S vacancies (N_{S1}) measured from the image. The density of the vacancies can be controlled by electron beam energy and dose[262]. **b** From left to right: atomic resolution STEM images of single-layer $MoSe_2$ when it is pristine, irradiated at 1×10^{15} He^+/cm^2 and 1×10^{16} He^+/cm^2, respectively[294]. **c** Left: STEM ADF image of a sample area with pristine single-layer MoS_2. Middle: STEM ADF image of the same area after being Ga^+ ion irradiated at 2.5×10^{13} Ga^+/cm^2. Right: Atomic resolution STEM images showing the ion beam created vacancies with different atomic configurations[295]. **d** Left: atomic resolution STEM ADF image of WS_2 without nitrogen plasma treatment. The S vacancies are highlighted by yellow arrows. Inset: zoomed-in view of part of the image to show the individual vacancies. Vacancy density is quantified using STEM images. Right: atomic resolution STEM ADF image of WS_2 after nitrogen plasma treatment. Inset: the corresponding electron diffraction pattern. The plasma treatment reduces the chalcogen vacancy density[277].

and automatization of the stacking process or developing assembly processes in high vacuum for improved cleanliness (Fig. 11b)[271,275,286,287], novel transfer approaches with a more precise control of vdW interactions between atomic layers need to be developed.

Outlook

Structural disorder and defects are inherent features in 2D TMDs, and they often profoundly affect the electrical and optical properties of the 2D structures. In this review, we have shown that a comprehensive understanding of the electrically and optically active structural defects has been gained over the last two decades. These defects modify the local electronic band structure and bonding characteristics, impacting charge transport, charge distribution, as well as light absorption and emission in 2D TMDs. A control of the defects can be realized via material fabrication, transfer, irradiation, implantation, and engineered strain. The utilization of the unique electrical and optical properties of 2D TMDs in future-generation device applications, for example, transistors, photodetectors, photovoltaics, and quantum information processing, relies on a detailed knowledge of the correlation between the defect structure and properties, as well as a knowledge of how to control the introduction of defects and structure distortions.

Despite the progress so far, applications of 2D TMDs still require a deeper understanding of the disorder-property relationships and technical issues related to a reproducible control of the disorder. For example, even if 2D TMDs are often found to be intrinsically n-doped, which is believed to be due to the ubiquitous presence of chalcogen vacancies, a direct correlation between the defect structure and doping characteristics has not been established. Moreover, SPEs have been observed in several 2D TMDs and appear to be a joint product of local strain and defects. However, a conclusive and detailed connection between the structure and SPE has not yet been established. The experimental observations regarding the effect of grain boundaries and edges on charge transport are not consistent. The

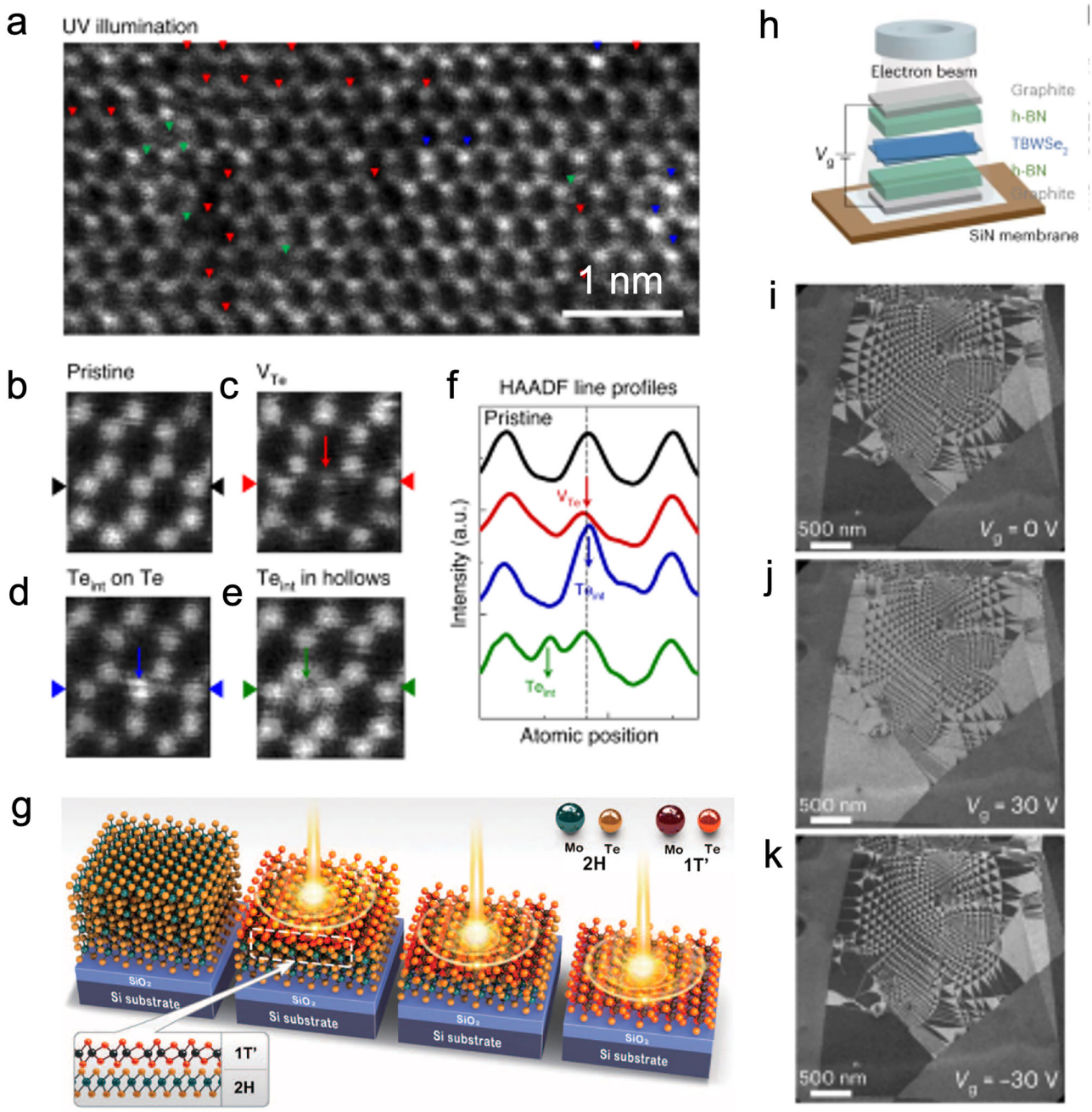

Fig. 10 | Controlling structural disorder using light and electric field. a Atomic resolution STEM image of UV-light-illuminated 2H-$MoTe_2$ crystals, where the representative point defects are marked with different colored arrows[279]. **b** STEM image of pristine $MoTe_2$[279]. **c** STEM image showing a Te vacancy (red arrow)[279]. **d** STEM image showing a Te interstitial (Te_{int}) on a Te site (blue arrow)[279]. **e** STEM image showing a Te_{int} at a hollow site (green arrow)[279]. **f** STEM image intensity line profiles along the marked directions (arrow heads) in (**b**–**e**)[279]. **g** Schematic of the process of laser-induced phase transition from 2H to 1T' in $MoTe_2$[280]. **h** Schematic of the 2D material stack used for in situ TEM investigation of electric field-induced domain dynamics in twisted bilayer WSe_2 ($TBWSe_2$)[284]. The $TBWSe_2$ is encapsulated between two h-BN layers. Graphite layers and h-BN act as an electron-beam-transparent gate electrode and insulating layer, respectively. The material stack is placed on an electron-transparent SiN window for TEM observations. V_g, gate voltage. **i**–**k** Dark field (DF) TEM images of twisted bilayer TMD taken at three different gate voltage conditions[284].

effect of stacking disorder on local charge distribution and correlation in 2D vdW heterostructures also remains to be explored, where unconventional properties due to local stacking disorder might emerge. To address these aspects, it is essential to perform correlative and in situ studies on the relationships between lattice structure, charge transport, and optical properties at the nanometer and atomic scales of the individual structure defects.

Moreover, our ability to accurately control the introduction of electrically and optically active defects in 2D TMDs is still limited and requires further development. The precise control of defect type, density, and distribution, which is critical for the applications of 2D TMDs in electronic and optoelectronic devices, has largely not been realized yet. Methods to remove anionic vacancies and accurately create and control their location and densities in the 2D crystals are yet to be established. Similarly, the possibility to accurately tune the dopant type and concentration in 2D TMDs via atom substitution in CVD growth or by ion implantation at the nanometer scale also needs to be further explored. Moreover, the mechanical stacking

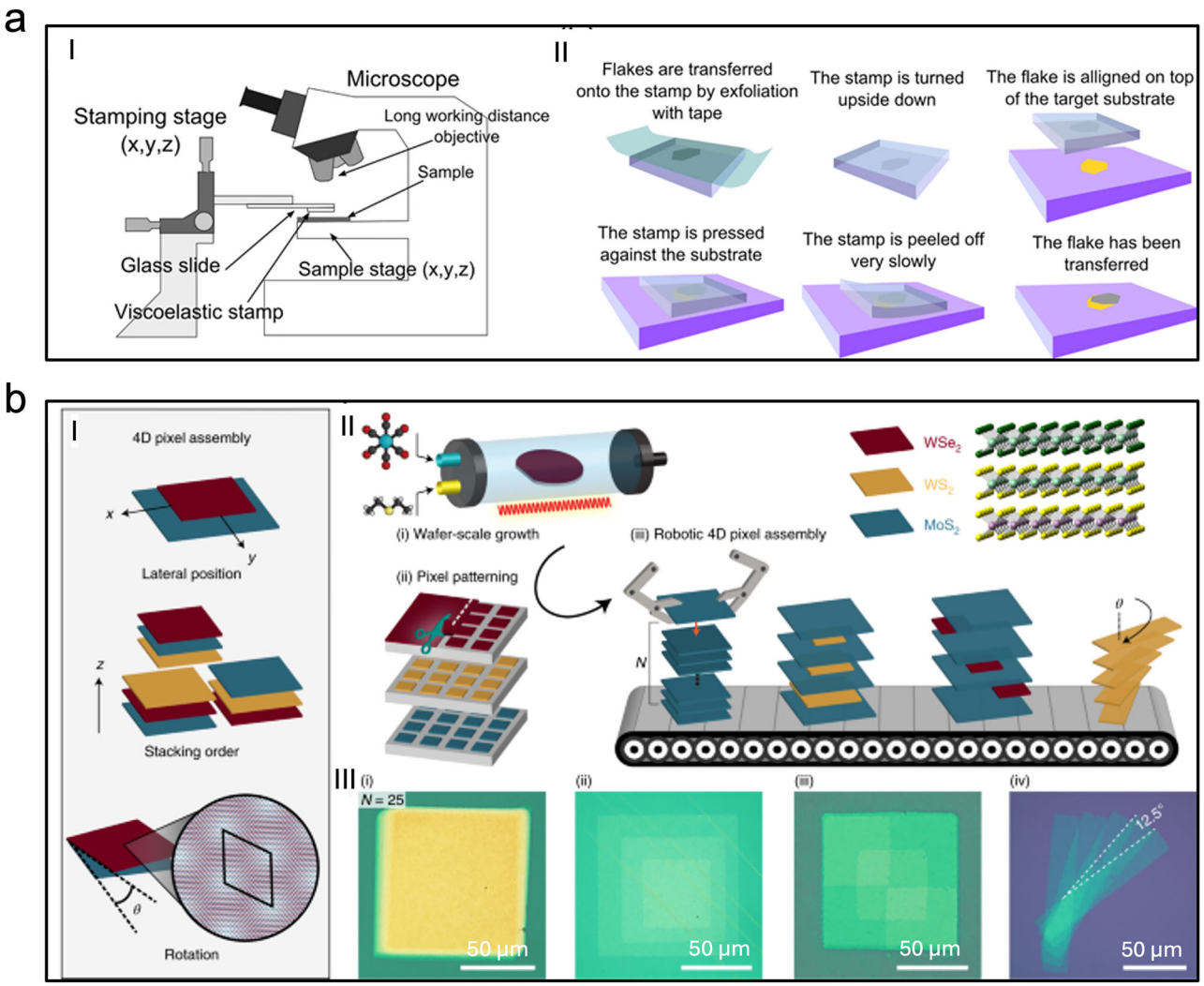

Fig. 11 | Mechanical transfer and stacking of 2D TMDs. a Commonly adopted deterministic mechanical transfer setup and process. (I) Schematic of the experimental setup employed for the all-dry transfer process. (II) Steps involved in the preparation of the viscoelastic polymer stamp (transfer substrate) and the deterministic transfer of an atomically thin flake onto a target substrate[285]. **b** Robotic pixel assembly of vdW heterostructures. (I) Schematic of the pixel assembly concept. (II) Production of pixels by wafer-scale growth (i), pixel patterning (ii), and automated pixel assembly of four conceptual structures by a robotic instrument (iii). (III) corresponding micrographs of vacuum-assembled robot-manufactured vdW heterostructures demonstrating layer number (i), composition (ii), lateral position (iii), and interlayer twist angle (iv) control[271].

approach for fabricating 2D heterostructures needs to be improved to increase the controllability and reproducibility, as well as to decrease stacking disorder. Novel transfer approaches with a more precise control of vdW interactions between individual atomic layers need to be developed. Regarding strain engineering, it is important to establish methods to apply strains up to the elastic limit of 2D TMDs in a reproducible, stable, and accurate manner. Local manipulation of strain gradients could provide a new way to create exotic electrical and optical properties in 2D TMDs. Reliable and quantitative strain measurements need to be combined with electrical and optical analysis with high spatial resolution to fully understand the strain effects. Strain effects on more complex structures than monolayers, such as heterostructures, have not been extensively exploited.

In conclusion, the effect of structural disorder and defects on the properties of 2D TMDs offers the potential of tailoring them for the next-generation devices in a wide range of applications. However, the knowledge about the defects and how they can reproducibly be introduced and controlled still needs to be further developed. Once established, the knowledge platform will initiate a new era in the fabrication of designed materials and devices. Moreover, the techniques and methods established for controlling structural disorder in 2D TMDs can be readily applied to other 2D materials, such as MXenes and 2D magnets.

Data availability

No datasets were generated or analyzed during the current study.

Received: 21 March 2025; Accepted: 26 November 2025;
Published online: 08 January 2026

References

1. Zhang, Y., Tan, Y. W., Stormer, H. L. & Kim, P. Experimental observation of the quantum Hall effect and Berry's phase in graphene. *Nature* **438**, 201–204 (2005).
2. Geim, A. K. & Novoselov, K. S. The rise of graphene. *Nat. Mater.* **6**, 183–191 (2007).
3. Novoselov, K. S. et al. Electric field in atomically thin carbon films. *Science* **306**, 666–669 (2004).
4. Castro Neto, A. H., Guinea, F., Peres, N. M. R., Novoselov, K. S. & Geim, A. K. The electronic properties of graphene. *Rev. Mod. Phys.* **81**, 109–162 (2009).

5. Cao, Y. et al. Unconventional superconductivity in magic-angle graphene superlattices. *Nature* **556**, 43–50 (2018).
6. Novoselov, K. S., Mishchenko, A., Carvalho, A. & Castro Neto, A. H. 2D materials and van der Waals heterostructures. *Science* **353**, aac9439 (2016).
7. Yankowitz, M. et al. Tuning superconductivity in twisted bilayer graphene. *Science* **363**, 1059–1064 (2019).
8. Britnell, L. et al. Strong light-matter interactions in heterostructures of atomically thin films. *Science* **340**, 1311–1314 (2013).
9. Akamatsu, T. et al. A van der Waals interface that creates in-plane polarization and a spontaneous photovoltaic effect. *Science* **372**, 68–72 (2021).
10. Barré, E. et al. Optical absorption of interlayer excitons in transition-metal dichalcogenide heterostructures. *Science* **376**, 6591 (2022).
11. Lu, X. et al. Superconductors, orbital magnets and correlated states in magic-angle bilayer graphene. *Nature* **574**, 653–657 (2019).
12. Fiori, G. et al. Electronics based on two-dimensional materials. *Nat. Nanotechnol.* **9**, 768–779 (2014).
13. Manzeli, S., Ovchinnikov, D., Pasquier, D., Yazyev, O. V. & Kis, A. 2D transition metal dichalcogenides. *Nat. Rev. Mater.* **2**, 1–15 (2017).
14. Wang, Q. H., Kalantar-Zadeh, K., Kis, A., Coleman, J. N. & Strano, M. S. Electronics and optoelectronics of two-dimensional transition metal dichalcogenides. *Nat. Nanotechnol.* **7**, 699–712 (2012).
15. Lee, C. H. et al. Atomically thin p-n junctions with van der Waals heterointerfaces. *Nat. Nanotechnol.* **9**, 676–681 (2014).
16. Radisavljevic, B., Radenovic, A., Brivio, J., Giacometti, V. & Kis, A. Single-layer MoS2 transistors. *Nat. Nanotechnol.* **6**, 147–150 (2011).
17. Regan, E. C. et al. Emerging exciton physics in transition metal dichalcogenide heterobilayers. *Nat. Rev. Mater.* **7**, 778–795 (2022).
18. Splendiani, A. et al. Emerging photoluminescence in monolayer MoS2. *Nano Lett.* **10**, 1271–1275 (2010).
19. Wang, G. et al. Colloquium: Excitons in atomically thin transition metal dichalcogenides. *Rev. Mod. Phys.* **90**, 021001 (2018).
20. Mak, K. F. & Shan, J. Photonics and optoelectronics of 2D semiconductor transition metal dichalcogenides. *Nat. Photonics* **10**, 216–226 (2016).
21. Wang, C., You, L., Cobden, D. & Wang, J. Towards two-dimensional van der Waals ferroelectrics. *Nat. Mater.* **22**, 542–552 (2023).
22. Novoselov, K. S. et al. Two-dimensional atomic crystals. *Proc. Natl. Acad. Sci. USA* **102**, 10451–10453 (2005).
23. Coleman, J. N. et al. Two-dimensional nanosheets produced by liquid exfoliation of layered materials. *Science* **331**, 568–571 (2011).
24. Smith, R. J. et al. Large-scale exfoliation of inorganic layered compounds in aqueous surfactant solutions. *Adv. Mater.* **23**, 3944–3948 (2011).
25. Zhan, Y., Liu, Z., Najmaei, S., Ajayan, P. M. & Lou, J. Large-area vapor-phase growth and characterization of MoS_2 atomic layers on a SiO_2 substrate. *Small* **8**, 966–971 (2012).
26. Liu, K. K. et al. Growth of large-area and highly crystalline MoS_2 thin layers on insulating substrates. *Nano Lett.* **12**, 1538–1544 (2012).
27. Kuc, A., Zibouche, N. & Heine, T. Influence of quantum confinement on the electronic structure of the transition metal sulfide TS_2. *Phys. Rev. B Condens. Matter Mater. Phys.* **83**, 245213 (2011).
28. Mak, K. F., Lee, C., Hone, J., Shan, J. & Heinz, T. F. Atomically thin MoS_2: a new direct-gap semiconductor. *Phys. Rev. Lett.* **105**, 136805 (2010).
29. Xia, F., Wang, H., Xiao, D., Dubey, M. & Ramasubramaniam, A. Two-dimensional material nanophotonics. *Nat. Photonics* **8**, 899–907 (2014).
30. Rivera, P. et al. Valley-polarized exciton dynamics in a 2D semiconductor heterostructure. *Science* **351**, 688–691 (2016).
31. Yu, H., Wang, Y., Tong, Q., Xu, X. & Yao, W. Anomalous light cones and valley optical selection rules of interlayer excitons in twisted heterobilayers. *Phys. Rev. Lett.* **115**, 187002 (2015).
32. Yin, Z. et al. Single-layer MoS_2 phototransistors. *ACS Nano* **6**, 74–80 (2012).
33. Li, M. et al. Imperfection-enabled memristive switching in van der Waals materials. *Nat. Electron.* **6**, 491–505 (2023).
34. Wang, H. et al. Integrated circuits based on bilayer MoS_2 transistors. *Nano Lett.* **12**, 4674–4680 (2012).
35. Geim, A. K. & Grigorieva, I. V. Van der Waals heterostructures. *Nature* **499**, 419–425 (2013).
36. Liu, Y. et al. Van der Waals heterostructures and devices. *Nat. Rev. Mater.* **1**, 1–17 (2016).
37. Radisavljevic, B. & Kis, A. Mobility engineering and a metal-insulator transition in monolayer MoS_2. *Nat. Mater.* **12**, 815–820 (2013).
38. Zhang, Q., Wee, A. T. S., Liang, Q., Zhao, X. & Liu, M. Defect engineering of two-dimensional transition-metal dichalcogenides: applications, challenges, and opportunities. *ACS Nano* **15**, 2165–2181 (2021).
39. Zhang, S. et al. Defect structure of localized excitons in a WSe_2 monolayer. *Phys. Rev. Lett.* **119**, 046101 (2017).
40. Rhodes, D., Chae, S. H., Ribeiro-Palau, R. & Hone, J. Disorder in van der Waals heterostructures of 2D materials. *Nat. Mater.* **18**, 541–549 (2019).
41. Zou, X. & Yakobson, B. I. An open canvas—2D materials with defects, disorder, and functionality. *Acc. Chem. Res* **48**, 73–80 (2015).
42. Luo, R. et al. Probing functional structures, defects, and interfaces of 2D transition metal dichalcogenides by electron microscopy. *Adv. Funct. Mater.* **34**, 2307625 (2024).
43. Zhou, W. et al. Intrinsic structural defects in monolayer molybdenum disulfide. *Nano Lett.* **13**, 2615–2622 (2013).
44. Liu, Z. et al. Identification of active atomic defects in a monolayered tungsten disulphide nanoribbon. *Nat. Commun.* **2**, 1–5 (2011).
45. Gyu Shin, B. et al. Indirect bandgap puddles in monolayer MoS_2 by substrate-induced local strain. *Adv. Mater.* **28**, 9378–9384 (2016).
46. Luo, Y. et al. In situ nanoscale imaging of moiré superlattices in twisted van der Waals heterostructures. *Nat. Commun.* **11**, 1–7 (2020).
47. McGilly, L. J. et al. Visualization of moiré superlattices. *Nat. Nanotechnol.* **15**, 580–584 (2020).
48. Weston, A. et al. Atomic reconstruction in twisted bilayers of transition metal dichalcogenides. *Nat. Nanotechnol.* **15**, 592–597 (2020).
49. Naik, M. H. & Jain, M. Ultraflatbands and shear solitons in Moiré patterns of twisted bilayer transition metal dichalcogenides. *Phys. Rev. Lett.* **121**, 266401 (2018).
50. Shabani, S. et al. Deep moiré potentials in twisted transition metal dichalcogenide bilayers. *Nat. Phys.* **17**, 720–725 (2021).
51. Regan, E. C. et al. Mott and generalized Wigner crystal states in WSe_2/WS_2 moiré superlattices. *Nature* **579**, 359–363 (2020).
52. Saito, R., Tatsumi, Y., Huang, S., Ling, X. & Dresselhaus, M. S. Raman spectroscopy of transition metal dichalcogenides. *J. Phys. Condens. Matter* **28**, 353002 (2016).
53. Zhang, X. et al. Phonon and Raman scattering of two-dimensional transition metal dichalcogenides from monolayer, multilayer to bulk material. *Chem. Soc. Rev.* **44**, 2757–2785 (2015).
54. Addou, R. & Wallace, R. M. Using photoelectron spectroscopy in the integration of 2D materials for advanced devices. *J. Electron Spectrosc. Relat. Phenom.* **231**, 94–103 (2019).
55. Chubarov, M., Choudhury, T. H., Zhang, X. & Redwing, J. M. In-plane x-ray diffraction for characterization of monolayer and few-layer transition metal dichalcogenide films. *Nanotechnology* **29**, 055706 (2018).
56. Su, S. et al. Scanning probe microscopies for characterizations of 2D materials. *Small Methods* **8**, 2400211 (2024).
57. Haider, M. et al. A spherical-aberration-corrected 200 kV transmission electron microscope. *Ultramicroscopy* **75**, 53–60 (1998).

58. Haider, M. et al. Electron microscopy image enhanced. *Nature* **392**, 768–769 (1998).
59. Batson, P. E., Dellby, N. & Krivanek, O. L. Sub-ångstrom resolution using aberration corrected electron optics. *Nature* **418**, 617–620 (2002).
60. Krivanek, O. L., Dellby, N. & Lupini, A. R. Towards sub-Å electron beams. *Ultramicroscopy* **78**, 1–11 (1999).
61. Hong, J. et al. Exploring atomic defects in molybdenum disulphide monolayers. *Nat. Commun.* **6**, 1–8 (2015).
62. Lin, Z. et al. Defect engineering of two-dimensional transition metal dichalcogenides. *2D Mater.* **3**, 022002 (2016).
63. Vancsó, P. et al. The intrinsic defect structure of exfoliated MoS_2 single layers revealed by scanning tunneling microscopy. *Sci. Rep.* **6**, 1–7 (2016).
64. Edelberg, D. et al. Approaching the intrinsic limit in transition metal diselenides via point defect control. *Nano Lett.* **19**, 4371–4379 (2019).
65. Lin, Y. C. et al. Realizing large-scale, electronic-grade two-dimensional semiconductors. *ACS Nano* **12**, 965–975 (2018).
66. Min, J., Kim, J. H. & Kang, J. Chalcogen vacancy engineering of two-dimensional transition metal dichalcogenides for electronic applications. *ACS Appl Nano Mater.* **7**, 26377–26396 (2023).
67. Wang, S., Robertson, A. & Warner, J. H. Atomic structure of defects and dopants in 2D layered transition metal dichalcogenides. *Chem. Soc. Rev.* **47**, 6764–6794 (2018).
68. Schuler, B. et al. Large spin-orbit splitting of deep in-gap defect states of engineered sulfur vacancies in monolayer WS_2. *Phys. Rev. Lett.* **123**, 076801 (2019).
69. McDonnell, S., Addou, R., Buie, C., Wallace, R. M. & Hinkle, C. L. Defect-dominated doping and contact resistance in MoS_2. *ACS Nano* **8**, 2880–2888 (2014).
70. Qiu, H. et al. Hopping transport through defect-induced localized states in molybdenum disulphide. *Nat. Commun.* **4**, 1–6 (2013).
71. Tosun, M. et al. Air-stable n-doping of WSe_2 by anion vacancy formation with mild plasma treatment. *ACS Nano* **10**, 6853–6860 (2016).
72. Zhang, X. et al. Single-atom vacancy doping in two-dimensional transition metal dichalcogenides. *Acc. Mater. Res.* **2**, 655–668 (2021).
73. Zhang, Z. et al. Optically active chalcogen vacancies in monolayer semiconductors. *Adv. Opt. Mater.* **10**, 2201350 (2022).
74. Chow, P. K. et al. Defect-induced photoluminescence in monolayer semiconducting transition metal dichalcogenides. *ACS Nano* **9**, 1520–1527 (2015).
75. Moody, G. et al. Microsecond valley lifetime of defect-bound excitons in monolayer WSe_2. *Phys. Rev. Lett.* **121**, 057403 (2018).
76. Xu, N. et al. Lattice vacancy induced energy renormalization of photonic quasiparticles in two-dimensional semiconductors. *ACS Nano* **17**, 16904–16911 (2023).
77. He, Y. M. et al. Single quantum emitters in monolayer semiconductors. *Nat. Nanotechnol.* **10**, 497–502 (2015).
78. Chakraborty, C., Kinnischtzke, L., Goodfellow, K. M., Beams, R. & Vamivakas, A. N. Voltage-controlled quantum light from an atomically thin semiconductor. *Nat. Nanotechnol.* **10**, 507–511 (2015).
79. Koperski, M. et al. Single photon emitters in exfoliated WSe_2 structures. *Nat. Nanotechnol.* **10**, 503–506 (2015).
80. Srivastava, A. et al. Optically active quantum dots in monolayer WSe_2. *Nat. Nanotechnol.* **10**, 491–496 (2015).
81. Palacios-Berraquero, C. et al. Large-scale quantum-emitter arrays in atomically thin semiconductors. *Nat. Commun.* **8**, 1–6 (2017).
82. Parto, K., Azzam, S. I., Banerjee, K. & Moody, G. Defect and strain engineering of monolayer WSe_2 enables site-controlled single-photon emission up to 150K. *Nat. Commun.* **12**, 1–8 (2021).
83. Klein, J. et al. Site-selectively generated photon emitters in monolayer MoS_2 via local helium ion irradiation. *Nat. Commun.* **10**, 1–8 (2019).
84. Singh, A. & Singh, A. K. Atypical behavior of intrinsic defects and promising dopants in two-dimensional WS_2. *Phys. Rev. Mater.* **5**, 084001 (2021).
85. Lin, Y.-C. et al. Controllable thin-film approaches for doping and alloying transition metal dichalcogenides monolayers. *Adv. Sci.* **8**, 2004249 (2021).
86. Li, H. et al. Growth of alloy $MoS_{2x}Se_{2(1-x)}$ nanosheets with fully tunable chemical compositions and optical properties. *J. Am. Chem. Soc.* **136**, 3756–3759 (2014).
87. Dumcenco, D. O., Kobayashi, H., Liu, Z., Huang, Y. S. & Suenaga, K. Visualization and quantification of transition metal atomic mixing in $Mo_{1-x}W_xS_2$ single layers. *Nat. Commun.* **4**, 1–5 (2013).
88. Ma, Q. et al. Postgrowth tuning of the bandgap of single-layer molybdenum disulfide films by sulfur/selenium exchange. *ACS Nano* **8**, 4672–4677 (2014).
89. Duan, X. et al. Synthesis of $WS_{2x}Se_{2-2x}$ alloy nanosheets with composition-tunable electronic properties. *Nano Lett.* **16**, 264–269 (2016).
90. Song, J. G. et al. Controllable synthesis of molybdenum tungsten disulfide alloy for vertically composition-controlled multilayer. *Nat. Commun.* **6**, 1–10 (2015).
91. Kang, H. S. et al. Bowing-alleviated continuous bandgap engineering of wafer-scale WS2xSe2(1-x) monolayer alloys and their assembly into hetero-multilayers. *NPG Asia Mater.* **14**, 1–11 (2022).
92. Liu, H., Antwi, K. K. A., Chua, S. & Chi, D. Vapor-phase growth and characterization of $Mo_{1-x}W_xS_2$ ($0 \le x \le 1$) atomic layers on 2-inch sapphire substrates. *Nanoscale* **6**, 624–629 (2013).
93. Chen, Y. et al. Tunable band gap photoluminescence from atomically thin transition-metal dichalcogenide alloys. *ACS Nano* **7**, 4610–4616 (2013).
94. Feng, Q. et al. Growth of large-area 2D $MoS_{2(1-x)}Se_{2x}$ semiconductor alloys. *Adv. Mater.* **26**, 2648–2653 (2014).
95. Fu, Q. et al. Synthesis and enhanced electrochemical catalytic performance of monolayer $WS_{2(1-x)}Se_{2x}$ with a tunable band gap. *Adv. Mater.* **27**, 4732–4738 (2015).
96. Lin, J. et al. Anisotropic ordering in 1T molybdenum and tungsten ditelluride layers alloyed with sulfur and selenium. *ACS Nano* **12**, 894–901 (2018).
97. Gong, Y. et al. Band gap engineering and layer-by-layer mapping of selenium-doped molybdenum disulfide. *Nano Lett.* **14**, 442–449 (2014).
98. Yang, S.-Z. et al. Rhenium-doped and stabilized MoS_2 atomic layers with basal-plane catalytic activity. *Adv. Mater.* **30**, 1803477 (2018).
99. Zhang, K. et al. Manganese doping of monolayer MoS_2: the substrate is critical. *Nano Lett.* **15**, 6586–6591 (2015).
100. Lin, Y.-C. et al. Properties of individual dopant atoms in single-layer MoS_2: atomic structure, migration, and enhanced reactivity. *Adv. Mater.* **26**, 2857–2861 (2014).
101. Gao, J. et al. Transition-metal substitution doping in synthetic atomically thin semiconductors. *Adv. Mater.* **28**, 9735–9743 (2016).
102. Suh, J. et al. Doping against the native propensity of MoS_2: degenerate hole doping by cation substitution. *Nano Lett.* **14**, 6976–6982 (2014).
103. Han, A. et al. One-step synthesis of single-site vanadium substitution in 1T-WS_2 monolayers for enhanced hydrogen evolution catalysis. *Nat. Commun.* **12**, 1–10 (2021).
104. Sasaki, S. et al. Growth and optical properties of Nb-doped WS_2 monolayers. *Appl. Phys. Express* **9**, 071201 (2016).
105. Robertson, A. W. et al. Atomic structure and spectroscopy of single metal (Cr, V) substitutional dopants in monolayer MoS_2. *ACS Nano* **10**, 10227–10236 (2016).

106. Liu, G. et al. MoS_2 monolayer catalyst doped with isolated Co atoms for the hydrodeoxygenation reaction. *Nat. Chem.* **9**, 810–816 (2017).
107. Lin, Y. C. et al. Revealing the atomic defects of WS_2 governing its distinct optical emissions. *Adv. Funct. Mater.* **28**, 1704210 (2018).
108. Munson, K. T. et al. Influence of rhenium concentration on charge doping and defect formation In MoS_2. *Adv. Electron Mater.* **11**, 2400403 (2024).
109. Li, Q. et al. Optimizing the atom substitution of Er in WS_2 nanosheets for high-performance photoelectrochemical applications. *J. Phys. Chem. C* **126**, 9293–9303 (2022).
110. Wang, L. et al. Enhanced visible-light response of ultrathin Er-doped MoS_2 nanosheets through a wet-chemical method. *J. Phys. Chem. C.* **127**, 1407–1414 (2023).
111. Wang, L., Zhang, S., Yan, L., Ji, X. & Zhang, Q. Chemical vapor deposition of Er-doped WS_2 flakes with near-infrared emission and enhanced near-infrared photoresponse. *J. Phys. Chem. C* **127**, 12678–12685 (2023).
112. Zhao, H. et al. Substantially enhanced properties of 2D WS_2 by high concentration of erbium doping against tungsten vacancy formation. *Research* **2022**, 9840970 (2022).
113. Liu, X. et al. Significantly improved optoelectronic performances of two-dimensional WS_2(Er3+)/WSe_2(Er3+) van der Waals heterojunctions. *Mater. Today Chem.* **38**, 102077 (2024).
114. Liu, S. et al. High photoresponse detectors based on Yb-doped monolayer WS_2 nanosheets. *Appl Surf. Sci.* **652**, 159287 (2024).
115. Ding, C. et al. Chemical vapor deposition growth of monolayer Er-doped molybdenum disulfide for efficient optoelectronic injection. *2D Mater.* **12**, 035001 (2025).
116. Bai, G. et al. 2D layered materials of rare-Earth Er-Doped MoS_2 with NIR-to-NIR down- and up-conversion photoluminescence. *Adv. Mater.* **28**, 7472–7477 (2016).
117. Ren, C. et al. Understanding dopant-host interactions on electronic structures and optical properties in Ce-doped WS_2 monolayers. *Adv. Funct. Mater.* **33**, 2301533 (2023).
118. Liu, S. et al. Supersensitive and broadband photodetectors based on high concentration of Er3+/Yb3+ Co-doped WS_2 monolayer. *Adv. Opt. Mater.* **12**, 2302229 (2024).
119. Liu, X. et al. Embedded lanthanoid ions modulated the periodic luminescence of transition metal dichalcogenide monolayers prepared from an aqueous orecursor. *J. Mater. Chem. C Mater.* **10**, 8061–8069 (2022).
120. Zhang, K. et al. Tuning the electronic and photonic properties of monolayer MoS_2 via in situ rhenium substitutional doping. *Adv. Funct. Mater.* **28**, 1706950 (2018).
121. Gao, H. et al. Tuning electrical conductance of MoS_2 monolayers through substitutional doping. *Nano Lett.* **20**, 4095–4101 (2020).
122. Azcatl, A. et al. Covalent nitrogen doping and compressive strain in MoS_2 by remote N_2 plasma exposure. *Nano Lett.* **16**, 5437–5443 (2016).
123. Nipane, A., Karmakar, D., Kaushik, N., Karande, S. & Lodha, S. Few-layer MoS_2 p-type devices enabled by selective doping using low energy phosphorus implantation. *ACS Nano* **10**, 2128–2137 (2016).
124. Frisenda, R., Molina-Mendoza, A. J., Mueller, T., Castellanos-Gomez, A. & Van Der Zant, H. S. J. Atomically thin p-n junctions based on two-dimensional materials. *Chem. Soc. Rev.* **47**, 3339–3358 (2018).
125. Zhu, K. et al. The development of integrated circuits based on two-dimensional materials. *Nat. Electron.* **4**, 775–785 (2021).
126. Liu, Y. et al. Promises and prospects of two-dimensional transistors. *Nature* **591**, 43–53 (2021).
127. Boland, C. S., Sun, Y. & Papageorgiou, D. G. Bandgap engineering of 2D materials toward high-performing straintronics. *Nano Lett.* **24**, 12722–12732 (2024).
128. Nassiri Nazif, K., Nitta, F. U., Daus, A., Saraswat, K. C. & Pop, E. Efficiency limit of transition metal dichalcogenide solar cells. *Commun. Phys.* **6**, 1–11 (2023).
129. Man, P., Srolovitz, D., Zhao, J. & Ly, T. H. Functional grain boundaries in two-dimensional transition-metal dichalcogenides. *Acc. Chem. Res* **54**, 4191–4202 (2021).
130. Van Der Zande, A. M. et al. Grains and grain boundaries in highly crystalline monolayer molybdenum disulphide. *Nat. Mater.* **12**, 554–561 (2013).
131. Ly, T. H. et al. Misorientation-angle-dependent electrical transport across molybdenum disulfide grain boundaries. *Nat. Commun.* **7**, 1–7 (2016).
132. Najmaei, S. et al. Vapour phase growth and grain boundary structure of molybdenum disulphide atomic layers. *Nat. Mater.* **12**, 754–759 (2013).
133. Guo, Z. et al. Intrinsic grain boundary structure and enhanced defect states in air-sensitive polycrystalline 1T'-WTe_2 monolayer. *Adv. Mater.* **36**, 2402219 (2024).
134. Huang, Y. L. et al. Gap states at low-angle grain boundaries in monolayer tungsten diselenide. *Nano Lett.* **16**, 3682–3688 (2016).
135. Batzill, M. Mirror twin grain boundaries in molybdenum dichalcogenides. *J. Phys. Condens. Matter* **30**, 493001 (2018).
136. Zhang, R. H. et al. In situ generation and manipulation of mirror twin boundaries in transition metal dichalcogenides. *Phys. Rev. B* **110**, L081407 (2024).
137. Komsa, H. P. & Krasheninnikov, A. V. Engineering the electronic properties of two-dimensional transition metal dichalcogenides by introducing mirror twin boundaries. *Adv. Electron Mater.* **3**, 1600468 (2017).
138. Zhou, Y. et al. Grain boundaries as electrical conduction channels in polycrystalline monolayer WS_2. *ACS Appl. Mater. Interfaces* **11**, 10189–10197 (2019).
139. Huang, Y. L. et al. Bandgap tunability at single-layer molybdenum disulphide grain boundaries. *Nat. Commun.* **6**, 1–8 (2015).
140. Wang, L. et al. Direct observation of one-dimensional Peierls-type charge density wave in twin boundaries of monolayer $MoTe_2$. *ACS Nano* **14**, 8299–8306 (2020).
141. Ambardar, S. et al. Probing chemical vapor deposition growth mechanism of polycrystalline $MoSe_2$ by near-field photoluminescence. *J. Phys. Chem. C* **126**, 13821–13829 (2022).
142. Wang, D. et al. Bandgap broadening at grain boundaries in single-layer MoS_2. *Nano Res.* **11**, 6102–6109 (2018).
143. Fu, W. et al. Toward edge engineering of two-dimensional layered transition-metal dichalcogenides by chemical vapor deposition. *ACS Nano* **17**, 16348–16368 (2023).
144. Chen, Q. et al. Atomically flat zigzag edges in monolayer MoS_2 by thermal annealing. *Nano Lett.* **17**, 5502–5507 (2017).
145. Zhao, X. et al. Mo-terminated edge reconstructions in nanoporous molybdenum disulfide film. *Nano Lett.* **18**, 482–490 (2018).
146. Bao, K. & Zhu, J. A brief review of reconstructions and electronic structures of MoS_2 zigzag edges. *J. Appl Phys.* **132**, 80702 (2022).
147. Gibertini, M. & Marzari, N. Emergence of one-dimensional wires of free carriers in transition-metal-dichalcogenide nanostructures. *Nano Lett.* **15**, 6229–6238 (2015).
148. Pan, H. & Zhang, Y. W. Edge-dependent structural, electronic and magnetic properties of MoS_2 nanoribbons. *J. Mater. Chem.* **22**, 7280–7290 (2012).
149. Li, Y., Zhou, Z., Zhang, S. & Chen, Z. MoS_2 nanoribbons: high stability and unusual electronic and magnetic properties. *J. Am. Chem. Soc.* **130**, 16739–16744 (2008).
150. Bollinger, M. V. et al. One-dimensional metallic edge states in MoS_2. *Phys. Rev. Lett.* **87**, 196803 (2001).
151. Huang, T. X. et al. Probing the edge-related properties of atomically thin MoS_2 at nanoscale. *Nat. Commun.* **10**, 1–8 (2019).
152. Zhang, C., Johnson, A., Hsu, C. L., Li, L. J. & Shih, C. K. Direct imaging of band profile in single layer MoS_2 on graphite: quasiparticle energy gap, metallic edge states, and edge band bending. *Nano Lett.* **14**, 2443–2447 (2014).

153. Wen, Y. et al. Mapping 1D confined electromagnetic edge states in 2D monolayer semiconducting MoS_2 using 4D-STEM. *ACS Nano* **16**, 6657–6665 (2022).
154. Shetty, N. et al. Scalable fabrication of edge contacts to 2D materials: implications for quantum resistance metrology and 2D electronics. *ACS Appl Nano Mater.* **6**, 6292–6298 (2023).
155. Choi, M. S. et al. Recent progress in 1D contacts for 2D-material-based devices. *Adv. Mater.* **34**, 2202408 (2022).
156. Parto, K. et al. One-dimensional edge contacts to two-dimensional transition-metal dichalcogenides: uncovering the role of Schottky-barrier anisotropy in charge transport across MoS_2/metal interfaces. *Phys. Rev. Appl* **15**, 064068 (2021).
157. Zheng, Y., Gao, J., Han, C. & Chen, W. Ohmic contact engineering for two-dimensional materials. *Cell Rep. Phys. Sci.* **2**, 100298 (2021).
158. Yin, X. et al. Edge nonlinear optics on a MoS_2 atomic monolayer. *Science* **344**, 488–490 (2014).
159. Chowdhury, T. et al. Substrate-directed synthesis of MoS_2 nanocrystals with tunable dimensionality and optical properties. *Nat. Nanotechnol.* **15**, 29–34 (2019).
160. Gutiérrez, H. R. et al. Extraordinary room-temperature photoluminescence in triangular WS_2 monolayers. *Nano Lett.* **13**, 3447–3454 (2013).
161. Lin, K. I. et al. Atom-dependent edge-enhanced second-harmonic generation on MoS_2 monolayers. *Nano Lett.* **18**, 793–797 (2018).
162. Uri, A. et al. Mapping the twist-angle disorder and Landau levels in magic-angle graphene. *Nature* **581**, 47–52 (2020).
163. Lau, C. N., Bockrath, M. W., Mak, K. F. & Zhang, F. Reproducibility in the fabrication and physics of moiré materials. *Nature* **602**, 41–50 (2022).
164. Lisi, S. et al. Observation of flat bands in twisted bilayer graphene. *Nat. Phys.* **17**, 189–193 (2020).
165. Sung, J. et al. Broken mirror symmetry in excitonic response of reconstructed domains in twisted $MoSe_2$/$MoSe_2$ bilayers. *Nat. Nanotechnol.* **15**, 750–754 (2020).
166. Hart, J. L. et al. Emergent layer stacking arrangements in c-axis confined $MoTe_2$. *Nat. Commun.* **14**, 1–9 (2023).
167. Deb, S. et al. Cumulative polarization in conductive interfacial ferroelectrics. *Nature* **612**, 465–469 (2022).
168. Andersen, T. I. et al. Excitons in a reconstructed moiré potential in twisted WSe_2/WSe_2 homobilayers. *Nat. Mater.* **20**, 480–487 (2021).
169. Tillotson, E. et al. Scanning electron microscopy imaging of twist domains in transition metal dichalcogenide heterostructures. *ACS Nano* **18**, 34033 (2024).
170. Van Winkle, M. et al. Rotational and dilational reconstruction in transition metal dichalcogenide moiré bilayers. *Nat. Commun.* **14**, 1–11 (2023).
171. Jin, C. et al. Observation of moiré excitons in WSe_2/WS_2 heterostructure superlattices. *Nature* **567**, 76–80 (2019).
172. Roldán, R., Castellanos-Gomez, A., Cappelluti, E. & Guinea, F. Strain engineering in semiconducting two-dimensional crystals. *J. Phys. Condens. Matter* **27**, 313201 (2015).
173. Dai, Z., Liu, L. & Zhang, Z. Strain engineering of 2D materials: issues and opportunities at the interface. *Adv. Mater.* **31**, 1805417 (2019).
174. Huang, T., Wei, W., Chen, X. & Dai, N. Strained 2D layered materials and heterojunctions. *Ann. Phys.* **531**, 1800465 (2019).
175. Peng, Z., Chen, X., Fan, Y., Srolovitz, D. J. & Lei, D. Strain engineering of 2D semiconductors and graphene: from strain fields to band-structure tuning and photonic applications. *Light Sci. Appl.* **9**, 1–25 (2020).
176. Lee, C. H. et al. Deep learning enabled strain mapping of single-atom defects in two-dimensional transition metal dichalcogenides with sub-picometer precision. *Nano Lett.* **20**, 3369–3377 (2020).
177. Azizi, A. et al. Defect coupling and sub-angstrom structural distortions in $W_{1-x}Mo_xS_2$ monolayers. *Nano Lett.* **17**, 2802–2808 (2017).
178. Han, Y. et al. Strain mapping of two-dimensional heterostructures with subpicometer precision. *Nano Lett.* **18**, 3746–3751 (2018).
179. Li, T. Ideal strength and phonon instability in single-layer MoS_2. *Phys. Rev. B Condens Matter Mater. Phys.* **85**, 235407 (2012).
180. Cooper, R. C. et al. Nonlinear elastic behavior of two-dimensional molybdenum disulfide. *Phys. Rev. B Condens Matter Mater. Phys.* **87**, 035423 (2013).
181. Bertolazzi, S., Brivio, J. & Kis, A. Stretching and breaking of ultrathin MoS_2. *ACS Nano* **5**, 9703–9709 (2011).
182. Zeng, L. et al. Tuning hole mobility of individual p-doped GaAs nanowires by uniaxial tensile stress. *Nano Lett.* **21**, 3894–3900 (2021).
183. Sun, Y., Thompson, S. E. & Nishida, T. Physics of strain effects in semiconductors and metal-oxide-semiconductor field-effect transistors. *J. Appl. Phys.* **101**, 104503 (2007).
184. Manzeli, S., Allain, A., Ghadimi, A. & Kis, A. Piezoresistivity and strain-induced band gap tuning in atomically thin MoS_2. *Nano Lett.* **15**, 5330–5335 (2015).
185. Island, J. O. et al. Precise and reversible band gap tuning in single-layer $MoSe_2$ by uniaxial strain. *Nanoscale* **8**, 2589–2593 (2016).
186. Chaves, A.et al. Bandgap engineering of two-dimensional semiconductor materials. *npj 2D Mater. Appl.* **4**, 29 (2020).
187. Desai, S. B. et al. Strain-induced indirect to direct bandgap transition in multilayer WSe_2. *Nano Lett.* **14**, 4592–4597 (2014).
188. Conley, H. J. et al. Bandgap engineering of strained monolayer and bilayer MoS_2. *Nano Lett.* **13**, 3626–3630 (2013).
189. Datye, I. M. et al. Strain-enhanced mobility of monolayer MoS_2. *Nano Lett.* **22**, 8052–8059 (2022).
190. Zhang, Y., Zhao, H. L., Huang, S., Hossain, M. A. & van der Zande, A. M. Enhancing carrier mobility in monolayer MoS_2 transistors with process-induced strain. *ACS Nano* **18**, 12377–12385 (2024).
191. Kayal, A. et al. Mobility enhancement in CVD-grown monolayer MoS_2 via patterned substrate-induced nonuniform straining. *Nano Lett.* **23**, 6629–6636 (2023).
192. Ng, H. K. et al. Improving carrier mobility in two-dimensional semiconductors with rippled materials. *Nat. Electron.* **5**, 489–496 (2022).
193. Dou, X., Ding, K., Jiang, D. & Sun, B. Tuning and identification of interband transitions in monolayer and bilayer molybdenum disulfide using hydrostatic pressure. *ACS Nano* **8**, 7458–7464 (2014).
194. Castellanos-Gomez, A. et al. Local strain engineering in atomically thin MoS_2. *Nano Lett.* **13**, 5361–5366 (2013).
195. Ryu, Y. K. et al. Microheater actuators as a versatile platform for strain engineering in 2D materials. *Nano Lett.* **20**, 5339–5345 (2020).
196. He, K., Poole, C., Mak, K. F. & Shan, J. Experimental demonstration of continuous electronic structure tuning via strain in atomically thin MoS2. *Nano Lett.* **13**, 2931–2936 (2013).
197. Wu, W. et al. Giant mechano-optoelectronic effect in an atomically thin semiconductor. *Nano Lett.* **18**, 2351–2357 (2018).
198. Maiti, R. et al. Strain-engineered high-responsivity $MoTe_2$ photodetector for silicon photonic integrated circuits. *Nat. Photonics* **14**, 578–584 (2020).
199. Hernández López, P. et al. Strain control of hybridization between dark and localized excitons in a 2D semiconductor. *Nat. Commun.* **13**, 1–9 (2022).
200. Abramov, A. N. et al. Photoluminescence imaging of single photon emitters within nanoscale strain profiles in monolayer WSe_2. *Nat. Commun.* **14**, 1–7 (2023).
201. Kim, G. et al. High-density, localized quantum emitters in strained 2D semiconductors. *ACS Nano* **16**, 9651–9659 (2022).
202. Puri, S. et al. Substrate interference and strain in the second-harmonic generation from $MoSe_2$ monolayers. *Nano Lett.* **24**, 13061–13067 (2024).
203. Schubert, E. F. *Doping in III-V Semiconductors* Cambridge Studies in Semiconductor Physics and Microelectronic Engineering (Cambridge University Press, 1993).

204. Bourgoin, J. & Lannoo, M. *Point Defects in Semiconductors II* (Springer Berlin, 2012).
205. Haller, E., Goulding, F. & Hilsum, C. *Handbook on Semiconductors* Vol. 4 (Elsevier, 1993).
206. Sun, Y., Thompson, S. E. & Nishida, T. *Strain Effect in Semiconductors: Theory and Device Applications* (Springer US, 2010).
207. Zhu, H. et al. Defects and surface structural stability of $MoTe_2$ under vacuum annealing. *ACS Nano* **11**, 11005–11014 (2017).
208. Liu, C. et al. Understanding epitaxial growth of two-dimensional materials and their homostructures. *Nat. Nanotechnol.* **19**, 907–918 (2024).
209. Kang, K. et al. High-mobility three-atom-thick semiconducting films with wafer-scale homogeneity. *Nature* **520**, 656–660 (2015).
210. Zhang, Y. et al. Recent progress in CVD growth of 2D transition metal dichalcogenides and related heterostructures. *Adv. Mater.* **31**, 1901694 (2019).
211. Yang, P. et al. Epitaxial growth of centimeter-scale single-crystal MoS_2 monolayer on Au(111). *ACS Nano* **14**, 5036–5045 (2020).
212. Cai, Z., Liu, B., Zou, X. & Cheng, H. M. Chemical vapor deposition growth and applications of two-dimensional materials and their heterostructures. *Chem. Rev.* **118**, 6091–6133 (2018).
213. Tang, L., Tan, J., Nong, H., Liu, B. & Cheng, H. M. Chemical vapor deposition growth of two-dimensional compound materials: controllability, material quality, and growth mechanism. *Acc. Mater. Res.* **2**, 36–47 (2021).
214. Zhao, Y. et al. Doping, contact and interface engineering of two-dimensional layered transition metal dichalcogenides transistors. *Adv. Funct. Mater.* **27**, 1603484 (2017).
215. Ding, S., Lin, F. & Jin, C. Quantify point defects in monolayer tungsten diselenide. *Nanotechnology* **32**, 255701 (2021).
216. Choi, S. H. et al. Is chemical vapor deposition of monolayer WSe_2 comparable to other synthetic routes? *APL Mater.* **11**, 111124 (2023).
217. Feng, S. et al. Synthesis of ultrahigh-quality monolayer molybdenum disulfide through in situ defect healing with thiol molecules. *Small* **16**, 2003357 (2020).
218. Wan, Y. et al. Low-defect-density WS_2 by hydroxide vapor phase deposition. *Nat. Commun.* **13**, 1–8 (2022).
219. Zuo, Y. et al. Robust growth of two-dimensional metal dichalcogenides and their alloys by active chalcogen monomer supply. *Nat. Commun.* **13**, 1–7 (2022).
220. Yang, P. et al. Epitaxial growth of inch-scale single-crystal transition metal dichalcogenides through the patching of unidirectionally orientated ribbons. *Nat. Commun.* **13**, 1–9 (2022).
221. Zhang, Y. et al. Controlled growth of high-quality monolayer WS_2 layers on sapphire and imaging its grain boundary. *ACS Nano* **7**, 8963–8971 (2013).
222. Liu, Z. et al. Strain and structure heterogeneity in MoS_2 atomic layers grown by chemical vapour deposition. *Nat. Commun.* **5**, 1–9 (2014).
223. Li, H. et al. Mechanical exfoliation and characterization of single- and few-layer nanosheets of WSe_2, TaS_2, and $TaSe_2$. *Small* **9**, 1974–1981 (2013).
224. Desai, S. B. et al. Gold-mediated exfoliation of ultralarge optoelectronically-perfect monolayers. *Adv. Mater.* **28**, 4053–4058 (2016).
225. Huang, Y. et al. Universal mechanical exfoliation of large-area 2D crystals. *Nat. Commun.* **11**, 1–9 (2020).
226. Velický, M. et al. Mechanism of gold-assisted exfoliation of centimeter-sized transition-metal dichalcogenide monolayers. *ACS Nano* **12**, 10463–10472 (2018).
227. Magda, G. Z. et al. Exfoliation of large-area transition metal chalcogenide single layers. *Sci. Rep.* **5**, 1–5 (2015).
228. Liu, F. et al. Disassembling 2D van der Waals crystals into macroscopic monolayers and reassembling into artificial lattices. *Science* **367**, 903–906 (2020).
229. Munkhbat, B. et al. Transition metal dichalcogenide metamaterials with atomic precision. *Nat. Commun.* **11**, 1–8 (2020).
230. Han, X., Lin, J., Liu, J., Wang, N. & Pan, D. Effects of hexagonal boron nitride encapsulation on the electronic structure of few-layer MoS_2. *J. Phys. Chem. C.* **123**, 14797–14802 (2019).
231. Kim, J. M. et al. Strained two-dimensional tungsten diselenide for mechanically tunable exciton transport. *Nat. Commun.* **15**, 1–9 (2024).
232. Branny, A., Kumar, S., Proux, R. & Gerardot, B. D. Deterministic strain-induced arrays of quantum emitters in a two-dimensional semiconductor. *Nat. Commun.* **8**, 1–7 (2017).
233. Zhang, Y., Choi, M. K., Haugstad, G., Tadmor, E. B. & Flannigan, D. J. Holey substrate-directed strain patterning in bilayer MoS_2. *ACS Nano* **15**, 20253–20260 (2021).
234. Wu, W. et al. Piezoelectricity of single-atomic-layer MoS_2 for energy conversion and piezotronics. *Nature* **514**, 470–474 (2014).
235. Frisenda, R. et al. Biaxial strain tuning of the optical properties of single-layer transition metal dichalcogenides. *npj 2D Mater. Appl.* **1**, 1–7 (2017).
236. Carrascoso, F., Frisenda, R. & Castellanos-Gomez, A. Biaxial versus uniaxial strain tuning of single-layer MoS_2. *Nano Mater. Sci.* **4**, 44–51 (2022).
237. Carrascoso, F., Li, H., Frisenda, R. & Castellanos-Gomez, A. Strain engineering in single-, bi- and tri-layer MoS_2, $MoSe_2$, WS_2 and WSe_2. *Nano Res.* **14**, 1698–1703 (2021).
238. Plechinger, G. et al. Control of biaxial strain in single-layer molybdenite using local thermal expansion of the substrate. *2d Mater.* **2**, 015006 (2015).
239. Li, Z. et al. Efficient strain modulation of 2D materials via polymer encapsulation. *Nat. Commun.* **11**, 1–8 (2020).
240. Carrascoso, F. et al. Improved strain engineering of 2D materials by adamantane plasma polymer encapsulation. *npj 2D Mater. Appl.* **7**, 1–8 (2023).
241. Zhu, H. et al. Observation of piezoelectricity in free-standing monolayer MoS_2. *Nat. Nanotechnol.* **10**, 151–155 (2015).
242. Rosenberger, M. R. et al. Quantum calligraphy: writing single-photon emitters in a two-dimensional materials platform. *ACS Nano* **13**, 904–912 (2019).
243. Qi, J. et al. Piezoelectric effect in chemical vapour deposition-grown atomic-monolayer triangular molybdenum disulfide piezotronics. *Nat. Commun.* **6**, 1–8 (2015).
244. Svensson, K., Jompol, Y., Olin, H. & Olsson, E. Compact design of a transmission electron microscope-scanning tunneling microscope holder with three-dimensional coarse motion. *Rev. Sci. Instrum.* **74**, 4945–4947 (2003).
245. Holmér, J. et al. An STM - SEM setup for characterizing photon and electron induced effects in single photovoltaic nanowires. *Nano Energy* **53**, 175–181 (2018).
246. Zeng, L. et al. The effect of bending deformation on charge transport and electron effective mass of p-doped GaAs nanowires. *Phys. status solidi Rapid Res. Lett.* **13**, 1900134 (2019).
247. Zheng, X. et al. Phase and polarization modulation in two-dimensional In_2Se_3 via in situ transmission electron microscopy. *Sci. Adv.* **8**, 773 (2022).
248. Wong, L. W. et al. Deciphering the ultra-high plasticity in metal monochalcogenides. *Nat. Mater.* **23**, 196–204 (2024).
249. Zhang, C. et al. Optomechanical properties of $MoSe_2$ nanosheets as revealed by in situ transmission electron microscopy. *Nano Lett.* **22**, 673–679 (2022).
250. Oviedo, J. P. et al. In situ TEM characterization of shear-stress-induced interlayer sliding in the cross section view of molybdenum disulfide. *ACS Nano* **9**, 1543–1551 (2015).
251. Zhao, Z. et al. Pressure induced metallization with absence of structural transition in layered molybdenum diselenide. *Nat. Commun.* **6**, 1–8 (2015).

252. Xia, J. et al. Strong coupling and pressure engineering in WSe_2-$MoSe_2$ heterobilayers. *Nat. Phys.* **17**, 92–98 (2020).
253. Wang, X. et al. Pressure-induced iso-structural phase transition and metallization in WSe_2. *Sci. Rep.* **7**, 1–9 (2017).
254. Xia, J. et al. Pressure-induced phase transition in Weyl semimetallic WTe_2. *Small* **13**, 1701887 (2017).
255. Yang, Y., Han, Y. & Li, R. Raman studies of two-dimensional Group-VI transition metal dichalcogenides under extreme conditions. *Crystals* **13**, 929 (2023).
256. Li, Y. et al. Structural and electronic properties of Weyl semimetal WTe_2 under high pressure. *J. Solid State Chem.* **323**, 124015 (2023).
257. Zeng, L. et al. Correlation between electrical transport and nanoscale strain in InAs/$In_{0.6}Ga_{0.4}As$ core-shell nanowires. *Nano Lett.* **18**, 4949–4956 (2018).
258. Hui, Y. Y. et al. Exceptional tunability of band energy in a compressively strained trilayer MoS_2 sheet. *ACS Nano* **7**, 7126–7131 (2013).
259. Cao, K. et al. Elastic straining of free-standing monolayer graphene. *Nat. Commun.* **11**, 1–7 (2020).
260. Espinosa, H. D., Bernal, R. A. & Filleter, T. In situ TEM electromechanical testing of nanowires and nanotubes. *Small* **8**, 3233–3252 (2012).
261. Ji, H., Song, Z., Wu, A., Zou, Y.-C. & Yang, G. Recent advances in the fundamentals and in situ characterizations for mechanics in 2D materials. *Nanoscale* **17**, 7574–7599 (2025).
262. Speckmann, C. et al. Combined electronic excitation and knock-on damage in monolayer MoS_2. *Phys. Rev. B* **107**, 094112 (2023).
263. Kretschmer, S., Lehnert, T., Kaiser, U. & Krasheninnikov, A. V. Formation of defects in two-dimensional MoS_2 in the transmission electron microscope at electron energies below the knock-on threshold: the role of electronic excitations. *Nano Lett.* **20**, 2865–2870 (2020).
264. Komsa, H. P. et al. Two-dimensional transition metal dichalcogenides under electron irradiation: defect production and doping. *Phys. Rev. Lett.* **109**, 035503 (2012).
265. Lehnert, T. et al. Electron-beam-driven structure evolution of single-layer $MoTe_2$ for quantum devices. *ACS Appl. Nano Mater.* **2**, 3262–3270 (2019).
266. Zograf, G. et al. Defect-assisted reversible phase transition in mono- and few-layer ReS_2. *npj 2D Mater. Appl.* **9**, 1–12 (2025).
267. Lin, J. et al. Flexible metallic nanowires with self-adaptive contacts to semiconducting transition-metal dichalcogenide monolayers. *Nat. Nanotechnol.* **9**, 436–442 (2014).
268. Inoue, A., Komori, T. & Shudo, K. I. Atomic-scale structures and electronic states of defects on Ar+-ion irradiated MoS_2. *J. Electron Spectrosc. Relat. Phenom.* **189**, 11–18 (2013).
269. Nan, H., Zhou, R., Gu, X., Xiao, S. & Ostrikov, K. K. Recent advances in plasma modification of 2D transition metal dichalcogenides. *Nanoscale* **11**, 19202–19213 (2019).
270. Tian, S. et al. Recent progress in plasma modification of 2D metal chalcogenides for electronic devices and optoelectronic devices. *Nanoscale* **16**, 1577–1599 (2024).
271. Mannix, A. J. et al. Robotic four-dimensional pixel assembly of van der Waals solids. *Nat. Nanotechnol.* **17**, 361–366 (2022).
272. Covarrubias, S. et al. A review on transfer methods of two-dimensional materials. *2D Mater.* **11**, 022004 (2024).
273. Pham, P. V. et al. Transfer of 2D films: from imperfection to perfection. *ACS Nano* **18**, 14841–14876 (2024).
274. Dean, C. R. et al. Boron nitride substrates for high-quality graphene electronics. *Nat. Nanotechnol.* **5**, 722–726 (2010).
275. Jaime Díez-Mé rida, A. et al. High-yield fabrication of bubble-free magic-angle twisted bilayer graphene devices with high twist-angle homogeneity. *Newton* **1**, 100007 (2025).
276. Vizner Stern, M., Salleh Atri, S. & Ben Shalom, M. Sliding van der Waals polytypes. *Nat. Rev. Phys.* **7**, 50–61 (2024).
277. Jiang, J. et al. A facile and effective method for patching sulfur vacancies of WS_2 via nitrogen plasma treatment. *Small* **15**, 1901791 (2019).
278. Wang, W., Jones, L. O., Chen, J. S., Schatz, G. C. & Ma, X. Utilizing ultraviolet photons to generate single-photon emitters in semiconductor monolayers. *ACS Nano* **16**, 21240–21247 (2022).
279. Seo, S. Y. et al. Reconfigurable photo-induced doping of two-dimensional van der Waals semiconductors using different photon energies. *Nat. Electron.* **4**, 38–44 (2020).
280. Cho, S. et al. Phase patterning for ohmic homojunction contact in $MoTe_2$. *Science* **349**, 625–628 (2015).
281. Castellanos-Gomez, A. et al. Laser-thinning of MoS_2: on demand generation of a single-layer semiconductor. *Nano Lett.* **12**, 3187–3192 (2012).
282. Wang, Y. et al. Structural phase transition in monolayer MoTe2 driven by electrostatic doping. *Nature* **550**, 487–491 (2017).
283. Zhang, F. et al. Electric-field induced structural transition in vertical $MoTe_2$- and $Mo_{1-x}W_xTe_2$-based resistive memories. *Nat. Mater.* **18**, 55–61 (2019).
284. Ko, K. et al. Operando electron microscopy investigation of polar domain dynamics in twisted van der Waals homobilayers. *Nat. Mater.* **22**, 992–998 (2023).
285. Castellanos-Gomez, A. et al. Deterministic transfer of two-dimensional materials by all-dry viscoelastic stamping. *2D Mater.* **1**, 011002 (2014).
286. Wang, W. et al. Clean assembly of van der Waals heterostructures using silicon nitride membranes. *Nat. Electron.* **6**, 981–990 (2023).
287. Masubuchi, S. et al. Autonomous robotic searching and assembly of two-dimensional crystals to build van der Waals superlattices. *Nat. Commun.* **9**, 1–12 (2018).
288. Ghorbani-Asl, M., Kretschmer, S. & Krasheninnikov, A. V. Chapter 9 - Two-dimensional materials under ion irradiation: from defectproduction to structure and property engineering. in Defects in Two-Dimensional Materials (eds Addou, R. & Colombo, L.) 259–301 (Elsevier, 2022). https://doi.org/10.1016/B978-0-12-820292-0.00015-X
289. Shen, Y. et al. In situ repair of 2D chalcogenides under electron beam irradiation. *Adv. Mater.* **30**, 1705954 (2018).
290. Wu, X., Luo, X., Cheng, H., Yang, R. & Chen, X. Recent progresses on ion beam irradiation induced structure and performance modulation of two-dimensional materials. *Nanoscale* **15**, 8925–8947 (2023).
291. Ozden, B. et al. Engineering vacancies for the creation of antisite defects in chemical vapor deposition grown monolayer MoS_2 and WS_2 via proton irradiation. *ACS Nano* **17**, 25101–25117 (2023).
292. Ahn, G. H. et al. Strain-engineered growth of two-dimensional materials. *Nat. Commun.* **8**, 1–8 (2017).
293. Pérez Garza, H. H., Kievit, E. W., Schneider, G. F. & Staufer, U. Controlled, reversible, and nondestructive generation of uniaxial extreme strains (>10%) in graphene. *Nano Lett.* **14**, 4107–4113 (2014).
294. Iberi, V. et al. Nanoforging single layer $MoSe_2$ through defect engineering with focused helium ion beams. *Sci. Rep.* **6**, 1–9 (2016).
295. Thiruraman, J. P. et al. Angstrom-size defect creation and ionic transport through pores in single-layer MoS_2. *Nano Lett.* **18**, 1651–1659 (2018).

Acknowledgements

L.J.Z. and E.O. acknowledge the financial support from the Knut and Alice Wallenberg Foundation (project 2019.0140) and the Swedish Research Council (project 2020-05432).

Author contributions

L.J.Z. and E.O. designed the structure of the manuscript. L.J.Z. wrote the manuscript. E.O. reviewed and edited the manuscript. All authors have read and approved the manuscript.

Funding

Open access funding provided by Chalmers University of Technology.

Competing interests

The authors declare no competing interests.

Additional information

Correspondence and requests for materials should be addressed to Lunjie Zeng or Eva Olsson.